https://doi.org/10.5194/amt-2019-204
Preprint. Discussion started: 6 August 2019

Atmospheric Measurement Techniques Discussions

A MAX-DOAS aerosol profile retrieval algorithm for high altitude measurements: application to measurements at Schneefernerhaus (UFS), Germany

Zhuoru Wang[1, 2], Ka Lok Chan[1], Klaus-Peter Heue[1], Adrian Doicu[1], Thomas Wagner[3], Robert Holla[4], and Matthias Wiegner[5]

[1]Remote Sensing Technology Institute, German Aerospace Center (DLR), Oberpfaffenhofen, Germany
[2]Faculty of Civil, Geo and Environmental Engineering, Technical University of Munich (TUM), Munich, Germany
[3]Max Planck Institute for Chemistry, Mainz, Germany
[4]German Meteorological Office (DWD), Hohenpeißenberg, Germany
[5]Meteorological Institute, Ludwig Maximilian University of Munich (LMU), Munich, Germany

Abstract. We present a new aerosol extinction profile retrieval algorithm for Multi-AXis Differential Optical Absorption Spectroscopy (MAX-DOAS) measurements at high altitude sites. The study is based on the long-term measurement (February 2012 to February 2016) at the Environmental Research Station Schneefernerhaus (UFS), Germany, which is located near the summit of Zugspitze, at an altitude of 2,650 m. Due to the low signal to noise ratio, commonly used MAX-DOAS retrieval algorithms based on the optimal estimation method are not suitable for the retrieval of high altitude measurements. We developed a new retrieval algorithm using an O_4 differential slant column density (DSCD) look-up table. The look-up table consists of simulated O_4 DSCDs corresponding to numerous possible aerosol extinction profiles. The sensitivities of O_4 absorption to several parameters were investigated for the design and parameterization of the look-up table. In the retrieval, the simulated O_4 DSCDs for each possible profile are derived by interpolating the look-up table to the observation geometries. The cost functions are calculated for each aerosol profile in the look-up table based on the simulated O_4 DSCDs, the O_4 DSCD observations as well as the measurement uncertainties. Valid profiles are selected from all the possible profiles according to the cost function, and the optimal solution is defined as the weighted mean of all valid profiles. A comprehensive error analysis is performed to better estimate the total uncertainty. Based on the assumption that the look-up table covers all the possible profiles under clear sky conditions, we determined a set of O_4 DSCD scaling factors for different elevation angles and wavelengths. The dependence of the scaling factors on elevation angle might be partly related to the specific properties of the high altitude station, e.g. the highly structured topography, horizontal gradients of the aerosol extinction and the systematic dependence of the surface albedo on altitude. The profiles retrieved from synthetic measurement data can well reproduce the true profile and the retrieval shows good stability to measurement noise. The aerosol optical depths (AODs) retrieved from the long-term measurement are compared to coincident and co-located sun photometer observations. High correlation coefficients of 0.733 and 0.798 are found for measurements at 360 and 477 nm, respectively. However, especially in summer the sun photometer AODs are systematically higher than the MAX-DOAS retrievals by a factor of 2. The discrepancy might be related to the limited measurement range of the MAX-DOAS, and is probably also related to the decreased sensitivity of the MAX-DOAS measurements at higher altitudes.

https://doi.org/10.5194/amt-2019-204
Preprint. Discussion started: 6 August 2019

Atmospheric Measurement Techniques Discussions

Our results also show maximum AOD and maximum Ångström exponent in summer which is consistent with observations from an AERONET station located ∼43 km of the MAX-DOAS.

1 Introduction

Atmospheric aerosols play an important role in the atmospheric physics and chemistry. They affect the atmospheric radiation budget by absorbing and scattering radiation, as well as providing nuclei for the formation of clouds (Haywood and Boucher, 2000; Bellouin et al., 2005; Li and Kou, 2011; Heald et al., 2014). Aerosols also have significant impacts on global climate change, local air quality and visibility (Bäumer et al., 2008; Levy II et al., 2013; Viana et al., 2014). Moreover, exposure to atmospheric aerosols can be harmful to human health (Valavanidis et al., 2008; Brook et al., 2010; Karanasiou et al., 2012). Besides primary aerosols which are directly introduced into the atmosphere, aerosols can also be secondarily formed through chemical reactions (Hinds, 2012). A significant increasing amount of anthropogenic aerosols and precursors have been released into the atmosphere since the industrial revolution (Liu et al., 1991; Junker and Liousse, 2008) which becomes a widely concerned environmental problem in recent years. Aerosols can be long-range transported and hence influence regions far from the sources (Wiegner et al., 2011; Almeida-Silva et al., 2013; Lee et al., 2013; Zhang et al., 2014; Chan and Chan, 2017; Chan, 2017; Chan et al., 2018). The properties and vertical distribution of aerosols vary strongly with time and location. Therefore, it is important to measure the spatial and temporal variations of aerosols for the better understanding of the role of aerosols in atmospheric processes. In addition, anthropogenic contribution to atmospheric aerosol load is one of the largest uncertainties in climate forcing assessments. Accurate measurements of aerosol optical properties are necessary for the further assessment of environmental and radiative effects of aerosols (Stocker et al., 2013).

Methodologies for aerosol monitoring are mature and well established: the backbone is certainly the AERONET network of sun photometers (Holben et al., 1998), complemented by active lidar remote sensing to provide range-resolved information. The latter includes research lidars (e.g., Pappalardo et al., 2014) and networks of ceilometers (e.g., Wiegner et al., 2014; Cazorla et al., 2017). Recently, the potential of Multi-AXis Differential Optical Absorption Spectroscopy (MAX-DOAS) for range-resolved aerosol retrievals was investigated as well (Platt and Stutz, 2008; Wagner et al., 2004; Frieß et al., 2006).

Ground-based MAX-DOAS is a remote sensing technique for measuring atmospheric aerosols and trace gases. MAX-DOAS instruments measure the spectra of scattered sunlight at several different viewing directions, and information of trace gas absorption along the light paths can be obtained by applying the differential optical absorption spectroscopy (DOAS) method to the ultraviolet-visible (UV-VIS) band. The retrieval of aerosols extinction profiles from MAX-DOAS measurements typically relies on the absorption signal of oxygen collision complex (O_4). As the vertical distribution profile of O_4 is well-known and stable, it is an ideal indicator for the atmospheric distribution of photon paths. Photon paths of scattered sunlight can be influenced by aerosols and hence change the measured O_4 slant columns. Therefore, aerosol vertical extinction profiles can be retrieved by fitting the O_4 observations to radiative transfer simulations. Since the experimental setup is relative simple and inexpensive, it has been widely used to measure the vertical distribution of atmospheric aerosols and trace gases in the past two decades (e.g., Hönninger et al., 2004; Irie et al., 2008; Li et al., 2010; Clémer et al., 2010; Frieß et al., 2011; Halla et al., 2011;

https://doi.org/10.5194/amt-2019-204
Preprint. Discussion started: 6 August 2019

Atmospheric Measurement Techniques Discussions

Irie et al., 2011; Vlemmix et al., 2011; Wagner et al., 2011; Li et al., 2013; Ma et al., 2013; Wang et al., 2014; Chan et al., 2015; Jin et al., 2016; Wang et al., 2016; Chan et al., 2017).

In the retrieval of vertical profile information from MAX-DOAS measurements, the aerosol profile is usually regarded as the state vector ($\boldsymbol{x}$) and the measured O_4 differential slant column densities (DSCDs) of each scanning cycle are regarded as the measurement vector ($\boldsymbol{y}$). The radiative transfer model used to simulate the O_4 DSCDs is regarded as the forward model ($\boldsymbol{F}$). As the radiative transfer in the atmosphere is non-linear, the retrieval is a non-linear problem. Moreover, the retrieval is ill-posed, which means the information contained in the observation is insufficient to determine a unique solution. In many of the other MAX-DOAS studies (e.g., Frieß et al., 2006; Clémer et al., 2010; Frieß et al., 2011; Irie et al., 2011; Wang et al., 2014, 2016; Chan et al., 2017), aerosol profiles are retrieved using the optimal estimation method (OEM) (Rodgers, 2000). The inversion of the aerosol profile is solved iteratively by minimizing the cost function. Vertical profile information can also be retrieved from MAX-DOAS observations using parameterized approaches (e.g., Lee et al., 2009; Li et al., 2010; Vlemmix et al., 2011; Wagner et al., 2011; Sinreich et al., 2013). These methods simplifies aerosol profiles with limited parameters, e.g., aerosol optical depth (AOD), layer height, shape parameter and etc. (Wagner et al., 2011; Hartl and Wenig, 2013). The optimal solution is usually determined by minimizing the difference between simulations and measurements.

However, as the retrieval is ill-posed and errors exist in both measurement and simulation, the profile with the lowest cost function may not be the one closest to the true profile. Moreover, in the typical OEM based algorithms, the iteration stops as soon as the cost function is smaller than a certain threshold. Therefore, the retrieved profile is not necessarily the one with the smallest cost function. At high altitude sites, the aerosol profile retrieval is more challenging, as the O_4 concentration as well as the aerosol load is much lower than at typical low altitude sites. The vertical gradient of aerosol extinction is also much smaller and the relative contributions from aerosols above the retrieval height to the total AOD are more significant. As a result, the signal to noise ratio (SNR) of such high altitude MAX-DOAS measurement is often insufficient to get a stable retrieval. Therefore, it is necessary to develop a dedicated MAX-DOAS aerosol profile retrieval algorithm for high altitude sites.

In this paper, we present a new MAX-DOAS aerosol profile retrieval algorithm dedicated for high altitude measurements. It is based on an O_4 DSCD look-up table. The look-up table includes simulated O_4 DSCDs corresponding to a very large number of aerosol extinction profiles. Our retrieval algorithm is applied to MAX-DOAS observations at the Environmental Research Station Schneefernerhaus (Umweltforschungsstation Schneefernerhaus, UFS). The UFS is located close to the summit of Zugspitze (2962 m), the highest mountain of Germany, at an altitude of 2,650 m. The O_4 concentration at Zugspitze is $\sim$40% lower compared to sea-level. As the measurement site is surrounded by the mountainous area of the Alps and far from polluted area, the aerosol load is much lower than at low altitude sites. The annual averaged AOD measured by the sun photometer at the UFS is around 0.1 at 350–500 nm. Moreover, the surface around the UFS is very complex which complicates the radiative transfer simulation. As a result, the model errors are larger compared to the flat and simple surfaces. In the study, we first analyzed the simulation uncertainty caused by the simplification of topography definition (see Section 3.3). Then we studied the sensitivity of O_4 to several parameters (see Section 3.4 and Appendix B). Based on the results, we designed the O_4 DSCD look-up table (see Section 3.5). The error estimation and inversion method are presented in the following sections. In Section

https://doi.org/10.5194/amt-2019-204
Preprint. Discussion started: 6 August 2019

Atmospheric Measurement Techniques Discussions

3.8, we present our method for determining the O_4 DSCD scaling factors based on the look-up table. Discussions of the retrieved aerosol profiles from the long-term measurements at the UFS are presented in Section 4.

2 Measurements

2.1 MAX-DOAS measurements

The MAX-DOAS instrument was set up on the platform on the 5th floor of the UFS (47.417°N, 10.980°E), about 20 m above ground level which is about 2,650 m about sea level. The instrument consists of a scanning telescope, a stepping motor controlling the viewing zenith angle of the telescope and two spectrometers covering both ultraviolet (UV) and visible (VIS) wavelength bands. Scattered sunlight collected by the telescope is redirected by a prism reflector and a quartz fiber bundle to the spectrometers for spectral analysis. The field of view (FOV) of the instrument is about 0.95°. Two spectrometers (OMT Instruments, OMT ctf-60) equipped with a CCD detector were used to cover both UV (320 – 478 nm) and VIS (427 – 649 nm) wavelength ranges. The full width half maximum (FWHM) spectral resolutions of the UV and VIS spectrometers are about 1.0 and 0.6 nm, respectively. The scanning direction of the telescope is controlled by the stepping motor.

As the scanning geometry is limited by the topography, the viewing azimuth angle of the telescope was adjusted to the due south (180°) with lowest elevation angle of 1°. A measurement sequence consists of measurements of scattered sunlight spectrum at elevation angles (α) of 90° (zenith), 30°, 20°, 10°, 5°, 2° and 1°. The exposure time and number of scans of each measurement are adjusted automatically depending on the intensity of received scattered sunlight in order to achieve similar intensity levels for all the measurements. A full measurement sequence takes about 10 min. The instrument takes measurements continuously during daytime (solar zenith angle (SZA) < 85°), but during the noon (175° < solar azimuth angle (SAA) <185°) and twilight periods (85° < SZA < 92°), the instrument takes only zenith measurements.

The MAX-DOAS is running since February 2012 until present. However, the measurement was interrupted between February 2013 and July 2013 due to instrument maintenance. In February 2016, the measurement was interrupted again and the VIS spectrometer was found to be degraded. In this paper, we present four years of MAX-DOAS measurements from February 2012 to February 2016.

2.2 Sun photometer measurements

Next to the MAX-DOAS instrument, a sun photometer was installed at the UFS, which provides measurements of radiative intensities at 12 wavelengths between 340 and 1640 nm with a temporal resolution of 1 s. The instrument was developed at the Meteorological Institute of Ludwig Maximilian University of Munich (LMU) based on a system operated in the framework of the SAMUM campaigns (Toledano et al., 2009, 2011) but with improved electronics and data acquisition developed by Physikalische Messsysteme Ltd. In this study, the AODs measured by the sun photometer were used for the inter-comparison with the MAX-DOAS retrieval. The AOD was determined applying the well-established Rayleigh calibration method. For this purpose, AOD measurements at 340 and 380 nm were interpolated to 360 nm while AODs at 477 nm were interpolated from

https://doi.org/10.5194/amt-2019-204
Preprint. Discussion started: 6 August 2019

Atmospheric Measurement Techniques Discussions

the measurements at 440 and 500 nm. Measurements were given as hourly averages in the time period between 10:00 UTC and 14:00 UTC. Only cloud-free conditions and periods of stable aerosol abundance (variability of intensities below 5% within one hour) were considered. These requirements reduce the number of available sun photometer measurements considerably. Note, that the AOD is often below 0.02 at the relevant wavelengths with an uncertainty due to calibration, Rayleigh correction, or radiometric accuracy in the order of ± 0.015. As a consequence the derivation of Ångström exponents is critical and thus omitted.

Aerosol optical properties not available from UFS-measurements but required for our MAX-DOAS inversion scheme (single scattering albedo and phase function) were estimated from the AERONET measurements at Hohenpeißenberg, which is located at an altitude of 980 m and approximately 43 km north of the UFS. These optical properties were available at 440, 675, 870 and 1020 nm, therefore, the data at 360 nm were extrapolated, and the data at 477 nm were interpolated.

3 Data analysis

3.1 Spectral analysis

The calibration of the spectrometers was preformed by fitting the measured solar spectra to the literature solar reference (Chance and Kurucz, 2010). All the measured spectra were first corrected for offset and dark current. The DOAS technique (Platt et al., 1979; Platt and Stutz, 2008) was applied to two wavelength ranges (338 – 370 nm for UV spectra and 440 – 490 nm for VIS spectra) each with strong O_4 absorption signal to retrieve the DSCDs of O_4. The DSCD is defined as the difference between the slant column densities (SCDs) of the off-zenith spectrum ($\alpha \neq 90°$) and the corresponding zenith reference spectrum ($\alpha = 90°$). For each scanning cycle, the zenith spectra before and after the cycle were temporally interpolated to the measurement time of each off-zenith spectrum. The broad band spectral structures caused by Rayleigh and Mie scattering were removed by including a low order polynomial in the DOAS fit. Absorption cross sections of several trace gases as well as a synthetic ring spectrum were included in the DOAS fit. Details of the DOAS fit settings for both bands are listed in Table 1. As the temperature at the UFS typically varies between 263 K and 279 K (Risius et al., 2015), trace gas absorption cross sections measured at 273 K were used in the DOAS fit. Small shift and squeeze of the wavelengths were allowed in the wavelength mapping process in order to compensate small uncertainties caused by the instability of the spectrograph. In this study, the spectra evaluation software QDOAS (version 3.2) developed by BIRA-IASB was used for the spectral fitting analysis.

3.2 Cloud screening

The aerosol profile retrieval requires the forward simulation of the radiative transfer in the atmosphere. As the radiative transfer is rather complicated for cloudy sky condition, the forward simulation usually assumes a cloud-free atmosphere. The aerosol retrieval might result in large uncertainty under cloudy or foggy conditions. Therefore, it is important to filter out the measurements taken under cloudy or foggy conditions. In this study, a colour index (CI) (Wagner et al., 2014, 2016) based cloud screening approach was applied to filter out cloudy measurements. The CI is defined as the ratio of radiative intensities at 330

https://doi.org/10.5194/amt-2019-204
Preprint. Discussion started: 6 August 2019

Atmospheric Measurement Techniques Discussions

Table 1. The DOAS fit settings for UV (338 – 370 nm) and VIS (440 – 490 nm) bands.

Species	Temperature	Fitting window		Reference
		338 – 370 nm (UV)	440 – 490 nm (VIS)	
CHOCHO	296 K		✓	Volkamer et al. (2005)
HCHO	273 K	✓		Chance and Orphal (2011)
H_2O	296 K	✓	✓	HITEMP 2010, Rothman et al. (2010)
NO_2 [(a)]	273 K	✓	✓	Bogumil et al. (2003)
NO_2 [(a)]	220 K	✓	✓	Bogumil et al. (2003)
O_3 [(b)]	273 K	✓	✓	Serdyuchenko et al. (2014)
O_3 [(b)]	223 K	✓	✓	Serdyuchenko et al. (2014)
O_4	293 K	✓	✓	Thalman and Volkamer (2013)
Ring		✓	✓	Chance and Spurr (1997)
Polynomial		5^{th} order	5^{th} order	
Intensity offset		linear	linear	

[(a)] I_0 correction is applied with SCD of 10^{17} molec/cm^2 (Aliwell et al., 2002).

[(b)] I_0 correction is applied with SCD of 10^{20} molec/cm^2 (Aliwell et al., 2002).

and 390 nm in this study. Larger CI indicates the UV/VIS intensity ratio is higher, hence, the sky is more blue. Our cloud screening method is presented in Appendix A. Based on our approach, ∼60% of the zenith measurements were determined as cloudy scenes, and the corresponding scanning cycles were not used in the following analysis.

3.3 Topography effect and the simplification in radiative transfer model

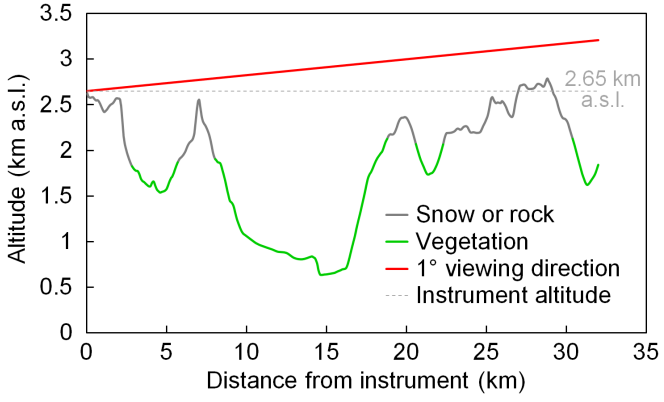

Figure 1. Altitude and type of the ground surface under the viewing direction (due south) of the MAX-DOAS at the UFS.

https://doi.org/10.5194/amt-2019-204
Preprint. Discussion started: 6 August 2019

Atmospheric Measurement Techniques Discussions

The topography around the UFS is quite complex, which complicates the radiative transfer simulations. Fig. 1 shows the topography under the viewing direction of the MAX-DOAS. The surface altitude varies between 600 and 2,800 m a.s.l. along the viewing direction of the MAX-DOAS instrument. Surface types include forests, meadows, rocks, etc. Some parts of the surface are seasonally or permanently covered by snow, while some steep slopes cannot be covered by snow even in winter.

Three-dimensional radiative transfer models (RTMs) can consider such a complex terrain, but they are computational expensive and unaffordable for retrieval. Due to the limitation of our RTM, we simplified the ground topography to a flat surface at an altitude of 2,650 m a.s.l. when calculating the look-up table described in Section 3.5. In order to compensate the error caused by this simplification, we investigated the error using the three-dimensional RTM TRACY-2.

TRACY-2 is a full spherical Monte-Carlo atmospheric RTM (Deutschmann, 2008; Wagner et al., 2007), which allows to simulate 3-dimensional radiative transport as well as 2-dimensional variation of the surface height. The model was compared to other RTMs and very good agreement was found (Wagner et al., 2007). For the simulations carried out in this study, a pseudo-reality topography was defined with the exact ground altitude in the azimuth direction of the MAX-DOAS measurements taken into account, whereas in the dimension orthogonal to this direction, the surface altitude was set constant. This simplification was chosen to reduce the computational effort. We feel that this approach is justified since the atmospheric light paths in the viewing direction of the instruments can be very large (up to several tens of kilometers), it is most important to take this variation of the surface altitude along this direction into account, whereas the influence of the orography perendicular to this direction is expected to be small.

Simulations were performed with all the combinations of three different SZAs (30°, 50° and 70°), three different relative solar azimuth angles (RAAs) (30°, 60° and 90°) and two different aerosol extinction profiles (an aerosol-free profile and a box-shape profile with AOD = 0.12 and box height = 3 km), i.e. altogether 18 cases. For each case, O_4 DSCDs at 360 and 477 nm were simulated with both the flat surface at 2,650 m and the pseudo-reality topography using TRACY-2. The relative errors of O_4 DSCDs simulated with the flat surface compared to those simulated with the pseudo-reality topography are calculated. A fixed surface albedo of 0.07 was used in the simulations. Fig. 2 shows the results of some of the cases: (a) and (b) shows the results of six cases with SZA = 50° and different RAAs and the both aerosol extinction profiles; (c) and (d) shows the results of six cases with RAA = 60° and different SZAs and the both aerosol extinction profiles.

As shown in all the panels of Fig. 2 as well as all the other cases which are not shown, O_4 DSCDs simulated with the flat surface are in general slightly underestimated compared to the pseudo-reality topography. The difference could be explained by the scattering in the valleys where the concentration of O_4 is higher. For the flat surface at 2,650 m, the light paths below 2,650 m would not be taken into account, and hence the O_4 DSCDs would be underestimated. Moreover, the relative error has no obvious correlation with elevation angle, SZA, RAA and aerosol load. This is because the light path below 2,650 m is influenced by the topography, and the influence differs with the observation geometry. In addition, the light path is also influenced by the aerosols above 2,650 m. Concerning the fact that only a pseudo-reality surface and a constant surface albedo is used in the study, the actual error caused by the topography simplification is expected to be much more complicated.

In order to make the compensation feasible, we consider the error as the combination of a systematic error and a random error. Based on the results of all the 18 cases of this study, the mean bias for each elevation angle and each wavelength is

https://doi.org/10.5194/amt-2019-204
Preprint. Discussion started: 6 August 2019

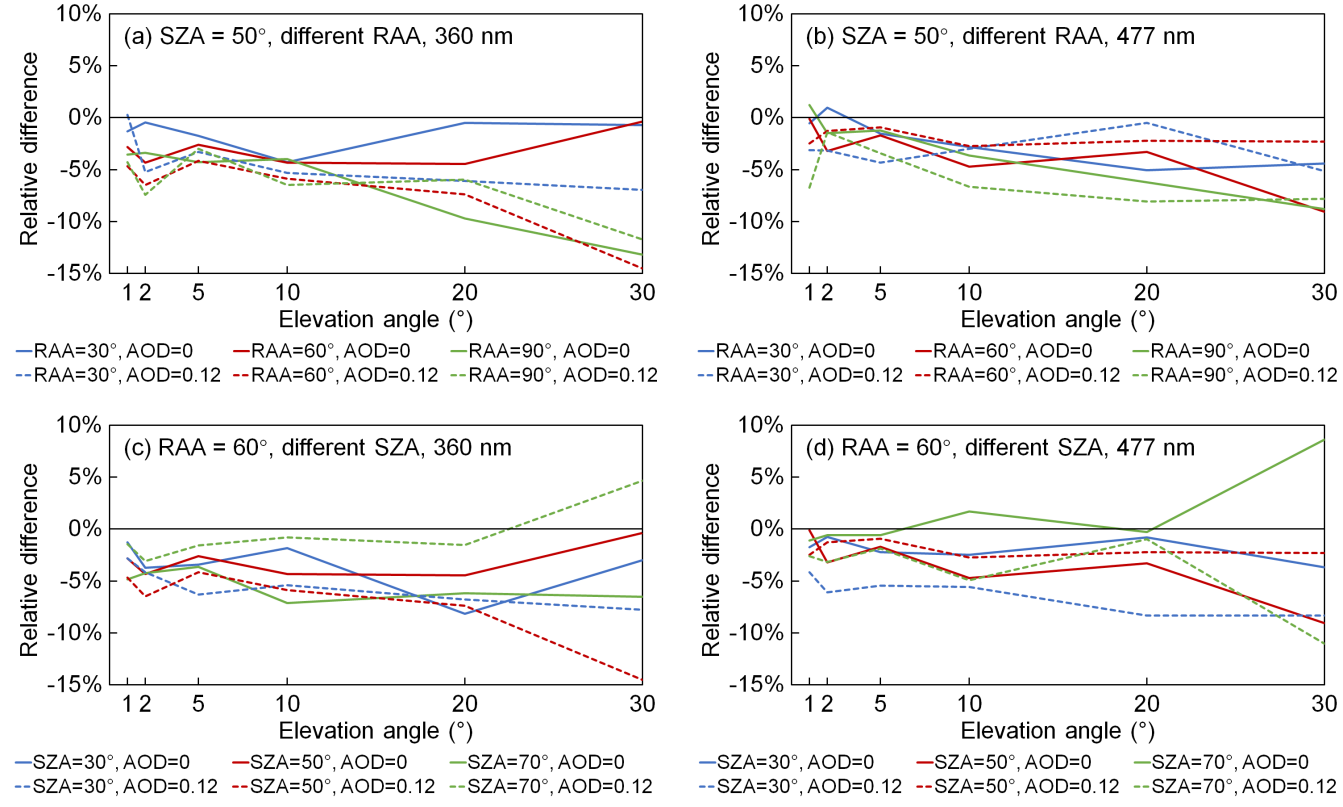

Figure 2. Relative differences of O_4 DSCDs at (a, c) 360 nm and (b, d) 477 nm simulated with a flat surface at 2,650 m comparing to the O_4 DSCDs simulated with the pseudo-reality topography. (a) and (b) show the results simulated with the same SZA of 50° and different RAAs (relative solar azimuth angles) of 30°, 60° and 90°; (c) and (d) show the results simulated with the same RAA of 60° and different SZAs of 30°, 50° and 70°. Solid curves are the results simulated under aerosol-free condition, and dashed curves are the results simulated with a box-shape profile with AOD = 0.12 and box height = 3 km.

considered as the systematic error, while the standard deviation of the relative difference is considered as the random error, see Table 2. In the aerosol profile retrieval, systematic errors are first corrected from the measured O_4 DSCDs, while random errors are included in the error budget in the calculation of cost function (see Section 3.6). In the following text, measured O_4 DSCDs refer to the values corrected by the systematic error unless otherwise mentioned.

3.4 Sensitivity analysis

In this study, the look-up table method is applied for the aerosol profile inversion. The look-up table consists of a number of possible aerosol extinction profiles and the corresponding simulated O_4 DSCDs for each elevation angle. In order to better formulate the look-up table, several sensitivity analyses were performed to determine the optimal vertical grid, step size of

https://doi.org/10.5194/amt-2019-204
Preprint. Discussion started: 6 August 2019

Atmospheric Measurement Techniques Discussions

Table 2. Systematic and random errors caused by the topography simplification. Results are calculated from the relative differences of O_4 DSCDs simulated with a flat surface at 2,650 m comparing to those simulated with the pseudo-reality surface in 18 cases (see text). The mean of the relative difference for each elevation angle and each wavelength is considered as the systematic error. The standard deviation of the relative difference is considered as the random error.

Elevation angle	UV (360 nm)		VIS (477 nm)	
	Systematic error (%)	Random error (%)	Systematic error (%)	Random error (%)
1°	-3.19	1.99	-2.30	2.24
2°	-3.69	1.64	-1.90	2.21
5°	-3.42	1.60	-2.48	1.57
10°	-4.12	2.32	-3.51	2.24
20°	-4.74	3.09	-3.93	4.63
30°	-5.08	5.44	-3.91	5.84

the aerosol extinction for each layer and the maximum aerosol extinction. In addition, these sensitivity analyses also help to understand the measurement and model errors which are very important for the aerosol profile inversion. The sensitivity analyses are based on the forward simulations of O_4 DSCDs using the radiative transfer model (RTM) LIDORT (Spurr et al., 2001; Spurr, 2008). We tested the sensitivity of O_4 absorption to surface albedo, aerosol optical properties, and the vertical distribution of aerosols. The results of the sensitivity analyses are shown in Appendix B.

3.5 Design of the look-up table

The basic idea of the look-up table method is to replace the repetitive time-consuming computation by a pre-calculated array. In this study, we replace the forward simulation of O_4 DSCDs by a look-up table, so that all the possible aerosol extinction profiles can be considered in the retrieval of each measurement cycle with an affordable computational effort.

We consider five input parameters for the forward simulation, which can be described as a function,

$$\Delta S_{\mathrm{s}} = f(\boldsymbol{x}, \lambda, \alpha, \theta, \phi), \tag{1}$$

where $\boldsymbol{x}$ is the aerosol extinction profile, λ represents the wavelength, α indicates the elevation angle, θ is the SZA, and ϕ represents the the RAA.

In order to create the look-up table, the input parameters need to be parametrized as a grid with finite nodes. We defined the grid based on the sensitivity and accuracy of the measurement. The aerosol extinction profile ($\boldsymbol{x}$) is parametrized as a profile set which consists of 7,553 possible profiles, see Section 3.5.1. As the simulated O_4 DSCDs are used to fit to the measured ones, only the data at 360 and 477 nm and at the six non-zenith elevation angles of our scanning cycle are included in the look-up table. SZA (θ) and RAA (ϕ) are parameterized as a grid with $1^\circ \times 1^\circ$ resolution. The look-up table includes 5,005 combinations of SZA and RAA, which can cover all the possible solar positions at the UFS. When we obtain data from the look-up table,

https://doi.org/10.5194/amt-2019-204
Preprint. Discussion started: 6 August 2019

Atmospheric Measurement Techniques Discussions

as the input SZA and RAA are not integers, the output ΔS_s is interpolated from the data of the four adjacent nodes of the SZA-RAA grid. In total, the five input parameters are parametrized as a grid with $7,553 \times 2 \times 6 \times 5,005 = 453,633,180$ nodes.

As discussed in Appendix B, O_4 DSCDs are also affected by other parameters such as the ground albedo, aerosol optical properties and etc., since their influences are relatively small and accurate data are not available, they are considered as uncertainties. In creating the look-up table, these parameters were fixed to the median values.

Details of the parameterization of the look-up table are summarized in Table 3. O_4 DSCDs corresponding to all the nodes of the look-up table were simulated using LIDORT.

Table 3. Parameters for calculating the O_4 DSCD look-up table.

Parameter	Symbol	Number of grid points	Grid values
aerosol extinction coefficient of 0 – 0.5 km above instrument (km^{-1})	σ_1	65	0, 0.001, 0.002, ..., 0.009, (0.001/step) 0.01, 0.0115, 0.013, ..., 0.0265, (0.0015/step) 0.028, 0.03, 0.032, ..., 0.038, (0.002/step) 0.04, 0.0425, 0.045, 0.0475, (0.0025/step) 0.05, 0.053, 0.056, ..., 0.077, (0.003/step) 0.08, 0.085, 0.09, ..., 0.115, (0.005/step) 0.12, 0.13, 0.14, ..., 0.19, (0.01/step) 0.2, 0.215, 0.23, 0.245, (0.015/step) 0.26, 0.28, 0.3 (0.02/step)
aerosol extinction coefficient of 0.5 – 1 km above instrument (km^{-1})	σ_2	14 ($\sigma_1 > 0$) 1 ($\sigma_1 = 0$)	0, $0.1\sigma_1$, $0.2\sigma_1$, ..., $1.3\sigma_1$ ($0.1\sigma_1$/step)
aerosol extinction coefficient of 1 – 2 km above instrument (km^{-1})	σ_3	9 ($\sigma_2 > 0$) 1 ($\sigma_2 = 0$)	0, $0.2\sigma_2$, $0.4\sigma_2$, $0.55\sigma_2$, $0.7\sigma_2$, $0.85\sigma_2$, σ_2, $1.15\sigma_2$, $1.3\sigma_2$
aerosol extinction coefficient of 2 – 4 km above instrument (km^{-1})		1	$0.5\sigma_3$
Wavelength (nm)	λ	2	360, 477
Elevation viewing angle (°)	α	6	1, 2, 5, 10, 20, 30
Solar zenith angle (SZA) (°)	θ	63	24, 25, 26, ..., 86 (1/step)
Relative solar azimuth angle (RAA) (°)	ϕ	122	0, 1, 2, ..., 121 (1/step)
Ground albedo		1	0.1
Single scattering albedo (SSA)		1	0.93 (360 nm) / 0.92 (477 nm)
Phase function		1	Median phase function[(a)] at Hohenpeißenberg obtained from AERONET

[(a)] The definition of the so-called median phase function is explained in Appendix B3.

https://doi.org/10.5194/amt-2019-204
Preprint. Discussion started: 6 August 2019

Atmospheric Measurement Techniques Discussions

3.5.1 Parameterization of the aerosol extinction profile

As discussed in Appendix B4, O_4 absorption is insensitive to the aerosols above 2 km. Therefore, our retrieval only focuses on aerosols between 0 and 2 km above the MAX-DOAS instrument (i.e. 2,650 – 4,650 m a.s.l.). In order to limit the complexity of the retrieval, avoid unreasonable results and make full use of the measurement sensitivity, we parameterize the aerosol extinction profile as aerosol extinction extinctions in three layers. The thicknesses of the two lower layers are defined as 0.5 km. Due to the lower sensitivity at high altitude, the thickness of the third layer is defined as 1 km. The aerosol profile is denoted as a 3-dimensional state vector,

$$\boldsymbol{x} = \begin{pmatrix} \sigma_1 \\ \sigma_2 \\ \sigma_3 \end{pmatrix}, \tag{2}$$

where σ_1 is the aerosol extinction coefficient between 0 and 0.5 km (2,650 – 3,150 m a.s.l.), σ_2 is the aerosol extinction coefficient between 0.5 and 1 km (3,150 – 3,650 m a.s.l.), and σ_3 is the aerosol extinction coefficient between 1 and 2 km (3,650 – 4,650 m a.s.l.).

A set of possible aerosol extinction profiles (denote as X_{LUT}) is defined for the look-up table. X_{LUT} is a finite set of $\boldsymbol{x}$, and the variation steps of σ_1, σ_2 and σ_3 are decided according to the sensitivity and accuracy of measurement. X_{LUT} includes only the profiles with reasonable shapes, and the variation range of σ_1, σ_2 and σ_3 covers the actual aerosol load under cloud-free condition.

As discussed in Appendix B6, the measurement sensitivity decreases with increasing surface aerosol extinction, and the sensitivity is very low when the surface aerosol extinction coefficient exceeds 0.3 km^{-1}. Therefore, σ_1 is set to vary between 0 and 0.3 km^{-1}. The variation step increases from 0.001 km^{-1} per step to 0.02 km^{-1} per step with increasing aerosol extinction, so that the difference of O_4 DSCD per step is similar to the typical spectral fitting error ($\sim$2%). In total, we define 65 values for σ_1, see Table 3.

The values of σ_2 are defined depending on σ_1. We have also looked into the co-located ceilometer observations at the UFS. The ceiometer data shows that it is rare to have strong elevated aerosol layers under cloud-free conditions. Therefore, we only allow weak elevated layers in designing the profile set. We assume that for reasonable profiles, σ_2 should not exceed σ_1 by more than 30%. According to the sensitivity, for each value of σ_1 ($\sigma_1 > 0$), we define 14 possible values for σ_2 which varies between 0 and $1.3\sigma_1$ with a step size of $0.1\sigma_1$. In case $\sigma_1 = 0$, elevated layers are not considered, then σ_2 and σ_3 can only be 0.

Similarly, the values of σ_3 are defined depending on σ_2, and σ_3 varies between 0 and $1.3\sigma_2$. Due to the lower measurement sensitivity at high altitude, we define 9 possible ratios between σ_3 and σ_2 (see Table 3). In case $\sigma_2 = 0$, then σ_3 can only be 0.

X_{LUT} includes the profiles with all the combinations of σ_1, $\frac{\sigma_2}{\sigma_1}$ and $\frac{\sigma_3}{\sigma_2}$, which consists of $1 + 64 \times [1 + (13 \times 9)] = 7{,}553$ aerosol extinction profiles in total.

https://doi.org/10.5194/amt-2019-204
Preprint. Discussion started: 6 August 2019

Atmospheric Measurement Techniques Discussions

As discussed in Appendix B4, the influence from the aerosols above 2 km is considered as a kind of uncertainty, and the aerosol extinction coefficient between 2 and 4 km is treated in a similar way as the ground albedo and aerosol optical properties. In the simulations for creating the look-up table, the aerosol extinction coefficient in this layer is always defined as $0.5\sigma_3$, so that this 'parameter' is set to the 'median' value. It should be noted that the aerosol extinction coefficient in this layer is not considered as a part of the retrieved profile.

3.6 Error estimation

Most of the other MAX-DOAS studies only consider the spectral fitting error in their retrieval. However, this fitting error only contributes to a small part of the total error. In addition, the total error is not directly proportional to the spectral fitting error. As the measurement and simulation uncertainties play an important part in our inversion method, we perform a comprehensive error analysis for the MAX-DOAS measurement and radiative transfer simulation of O_4 DSCDs. In this study, error from seven major sources are taken into account in estimating the total uncertainty.

3.6.1 DOAS fitting error

The DOAS fitting error is denoted as ϵ_{fit}. In this study, ϵ_{fit} is obtained from the fitting error reported by QDOAS which is based on the analysis of the spectral fit residual. For the low elevation angles (1°, 2°, 5°), the percentage of ϵ_{fit} comparing to the DSCD typically varies between 1% and 3% at the UV band and between 0.3% and 0.7% at the VIS band, which is rather small compared to other sources of error. However, for the elevation angle of 30°, as the absolute DSCD value is much smaller, the percentage of ϵ_{fit} can be up to $\sim$10% and $\sim$25% at the UV and VIS bands, respectively.

3.6.2 Error caused by temperature

The error caused by temperature is denoted as ϵ_{temp}. As discussed in Section 3.1, O_4 absorption cross section measured at 273 K is used in the DOAS fitting. However, the effective temperature of the MAX-DOAS measurements could be significantly different from 273 K. Previous studies show that O_4 absorption has a strong and systematic dependence on temperature (Thalman and Volkamer, 2013; Wagner et al., 2018).

In order to estimate ϵ_{temp}, we compared the O_4 DSCDs retrieved using absorption cross sections measured at 253 K and 293 K to those retrieved with cross section measured at 273 K. The comparison shows that the O_4 DSCDs are underestimated by 5.1% at the UV band and 2.5% at the VIS band when the effective temperature is 293 K. On the other hand, the O_4 DSCDs are overestimated by 6.9% at the UV band and 3.9% at the VIS band when the effective temperature is 253 K. These systematic errors are almost constant, regardless of the observation geometry. Between 253 and 293 K, the average variation rate of O_4 DSCD at UV band is 0.3% / K. This result is in general agreement with Wagner et al. (2018). They found that with the fitting window of 352 – 387 nm, O_4 DSCDs retrieved using the cross section at 203 K are reported to be 30% smaller than those retrieved using the cross section at 293 K, i.e. 0.33% / K in average.

https://doi.org/10.5194/amt-2019-204
Preprint. Discussion started: 6 August 2019


Atmospheric Measurement Techniques Discussions

Based on the fact that the temperature at the measurement site varies between ∼258 and 288 K during daytime in most cases, we estimate the ϵ_{temp} of all measurements as 4.5% and 2.4% of the O_4 DSCD at UV and VIS band, respectively.

3.6.3 Random error caused by the definition of the topography

The random error caused by the simplification of the topography definition is denoted as ϵ_{topo}. As discussed in Section 3.3, the standard deviation of the relative errors at each elevation angle and each wavelength from the 18 cases are treated as ϵ_{topo}. ϵ_{topo} for each elevation angle and each band is shown in Table 2.

3.6.4 Error caused by surface albedo

The error caused by surface albedo is denoted as ϵ_{SA}. As discussed in B1, ϵ_{SA} is different under different observation geometries and different aerosol loads. Therefore, we use a simple look-up table to determine ϵ_{SA}.

According to further sensitivity tests, ϵ_{SA} is insensitive to vertical distribution of aerosols. In order to simplify the error estimation, we assume that it is only influenced by the AOD. In addition, from the O_4 DSCD look-up table, we found that O_4 DSCD at 5° is almost negatively correlated with AOD, while it is insensitive to the shape of profile. Therefore, we use the O_4 DSCD measured at 5° as the indicator for estimating the AOD.

The ϵ_{SA} look-up table consists of the ϵ_{SA} for all the combinations of SZA and RAA (with $1^\circ \times 1^\circ$ resolution) and 65 profiles of the X_{LUT} with $\sigma_1 = \sigma_2 = \sigma_3$. Same as the O_4 DSCD look-up table, the aerosol extinction coefficient between 2 and 4 km is set as $0.5\sigma_3$. O_4 DSCDs were simulated with both the median and extreme values of surface albedo (0.1 and 0.2, respectively). The relative difference between the two simulations is considered as the error.

In order to determine ϵ_{SA} of each measurement, the AOD is first estimated using the O_4 DSCD measured at 5° of the corresponding scan. Subsequently, ϵ_{SA} is derived from the look-up table according to the first approximation of AOD.

It should be noted that there is probably also a systematic effect of the surface albedo on the measurements at the high altitude station: due to the dependence of the snow coverage on altitude, the surface albedo close to the instrument is typically higher than at locations far away. Since the measurements at high elevation angles are usually more sensitive to air masses closer to the instrument, they are probably stronger affected by snow and ice than measurements at low elevation angles. In this study, this effect cannot be further quantified, but it might be one reason for the need of different O_4 DSCD scaling factors for different elevation angles, see Section 3.8.

3.6.5 Error caused by single scattering albedo

The error caused by SSA is denoted as ϵ_{SSA}. Similar to ϵ_{SA}, ϵ_{SSA} is determined using a simple look-up table. The error values were also calculated from the relative differences between O_4 DSCDs simulated under extreme and median values of SSA. As discussed in Appendix B2 and shown in Fig. B2, the extreme value is chosen as 0.997 for both the UV and VIS bands, while the median value is chosen as 0.92 for the UV band and 0.93 for the VIS band, respectively.

https://doi.org/10.5194/amt-2019-204
Preprint. Discussion started: 6 August 2019

Atmospheric Measurement Techniques Discussions

3.6.6 Error caused by phase function

The error caused by phase function is denoted as ϵ_{PF}. ϵ_{PF} is also determined using a simple look-up table. As discussed in Appendix B3, from all phase functions measured by the AERONET station in Hohenpeißenberg during the period of 2013 – 2014, the phase function with which the simulated O_4 DSCDs at all elevation angles are closest to the median values is chosen as the 'median' phase function. The phase function with which the simulated O_4 DSCDs are closest to the rank of 95% (i.e. 2σ) is chosen as the 'extreme' phase function. The difference of O_4 DSCDs between the simulations with 'median' and 'extreme' phase function is treated as ϵ_{PF}.

3.6.7 Error caused by aerosols above retrieval height

The error caused by aerosols above retrieval height (2 km above instrument) is denoted as $\epsilon_{\text{2-4 km}}$. As discussed in B5, $\epsilon_{\text{2-4 km}}$ is treated similarly as ϵ_{SA}, ϵ_{SSA} and ϵ_{PF}, and it is also determined using a simple look-up table. The error values are calculated from the relative differences between O_4 DSCDs simulated with profiles with the aerosol extinction coefficient between 2 and 4 km equals to σ_3 and those simulated with profiles with the aerosol extinction coefficient between 2 and 4 km equals to $0.5\sigma_3$.

3.6.8 Total uncertainty

We assume that all the seven kinds of error follow the normal distribution, and the total uncertainty of each band and each elevation angle can be determined by the root mean square of the seven errors as

$$\epsilon = \sqrt{\epsilon_{\mathrm{fit}}^2 + \epsilon_{\mathrm{temp}}^2 + \epsilon_{\mathrm{topo}}^2 + \epsilon_{\mathrm{SA}}^2 + \epsilon_{\mathrm{SSA}}^2 + \epsilon_{\mathrm{PF}}^2 + \epsilon_{\text{2-4 km}}^2}. \tag{3}$$

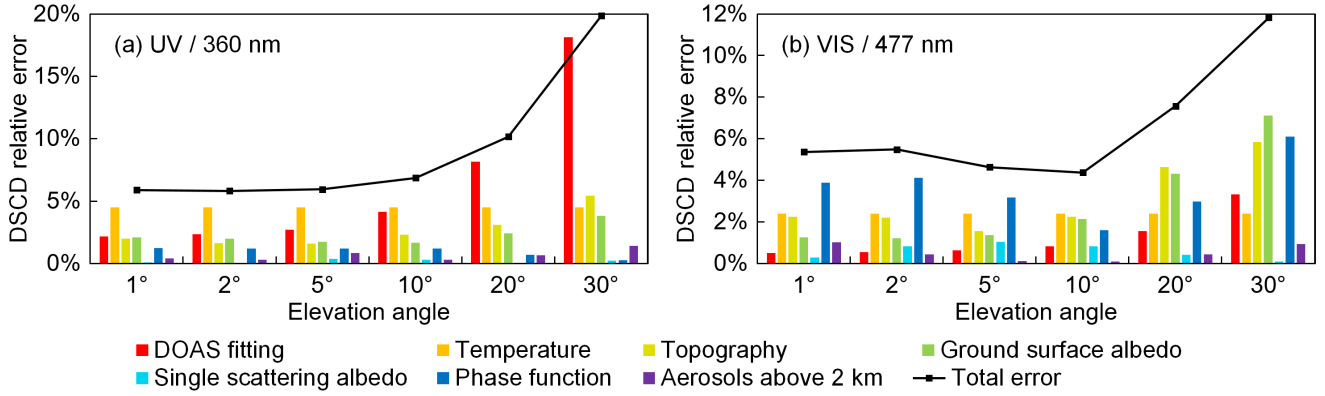

Figure 3. Error budget of (a) UV and (b) VIS bands of the scanning cycle on 07 Dec 2015 at ∼13:55 UTC. Y-axis refer to the relative error of O_4 DSCDs.

https://doi.org/10.5194/amt-2019-204
Preprint. Discussion started: 6 August 2019

Atmospheric Measurement Techniques Discussions

Fig. 3 shows an example of the error budget of a scanning cycle for both wavelength bands. The result shows that the major source of error is different at different elevation angles and different wavelengths.

3.6.9 Other possible error sources

Besides the seven above-mentioned error sources, there are still some other sources of error which are difficult to be estimated and hence not included in the error estimation. For example:

a. Error in O_4 DSCD scaling factors: in this study, we found that an elevation dependent O_4 DSCD scaling factor is needed to bring measurements and model results into agreement. We determined the factors based on the statistical analysis of the long-term measurement, see Section 3.8. However, as it is still difficult to estimate the uncertainties of the scaling factors, they are currently not taken into account in calculating the total uncertainty.

b. Error caused by horizontal gradients of the aerosol extinction: besides its direct effect on the measurements, the complex topography might also cause systematic horizontal gradients of the aerosol extinction. For example polluted air masses from the valleys might be transported to higher altitudes according to the vertical mixing and the prevailing wind direction. Such effects can be especially important for the measurements discussed here because of the rather low AOD. Further quantification of the effects of possible horizontal gradients is beyond the scope of this study, but might be one reason for the observed elevation dependence of the O_4 DSCD scaling factor.

In order to avoid the underestimation of the measurement uncertainty, we set a relative relaxed threshold of cost functions for choosing valid profiles, see Section 3.7.

3.7 Inversion method

Aerosol extinction profiles are retrieved from the measured O_4 DSCDs of each scanning cycle. UV and VIS band measurements are retrieved separately. The measured O_4 DSCDs of UV and VIS bands are fitted to the simulated O_4 DSCDs at 360 and 477 nm, respectively. In the retrieval, we assume the state of atmosphere is stable during a scanning cycle and the distribution of aerosols is homogeneous in horizontal direction. For a single scanning cycle and a single O_4 wavelength band λ, the measured O_4 DSCDs are denoted as a measurement vector

$$\boldsymbol{y}_{\mathrm{m}} = \begin{pmatrix} \Delta S_{\lambda,1} \\ \Delta S_{\lambda,2} \\ \vdots \\ \Delta S_{\lambda,M} \end{pmatrix}, \tag{4}$$

where M is the number of off-zenith measurements in each scanning cycle, which is 6 in this study. $\Delta S_{\lambda,1}$, $\Delta S_{\lambda,2}$, ..., $\Delta S_{\lambda,6}$ are the O_4 DSCDs measured at O_4 wavelength band λ with the viewing elevation angles of 1°, 2°, 5°, 10°, 20° and 30°, respectively.

https://doi.org/10.5194/amt-2019-204
Preprint. Discussion started: 6 August 2019

Atmospheric Measurement Techniques Discussions

The simulated O_4 DSCDs corresponding to each possible aerosol extinction profile in X_{LUT} can be obtained from the look-up table. Similar to $\boldsymbol{y}_{\mathrm{m}}$, the simulation vector $\boldsymbol{y}_{\mathrm{s}}$ for each possible profile $\boldsymbol{x}$ is be denoted as

$$\boldsymbol{y}_{\mathrm{s}}(\boldsymbol{x}) = \begin{pmatrix} f(\boldsymbol{x},\lambda,\alpha_1,\theta_1,\phi_1) \\ f(\boldsymbol{x},\lambda,\alpha_2,\theta_2,\phi_2) \\ \vdots \\ f(\boldsymbol{x},\lambda,\alpha_M,\theta_M,\phi_M) \end{pmatrix}, \boldsymbol{x} \in X_{\mathrm{LUT}}. \tag{5}$$

Aerosol extinction profiles can be derived by fitting the forward simulation to the measured O_4 DSCDs. Typically, the optimal solution can be detemined by minimizing the cost function, which is defined as

$$\chi^2(\boldsymbol{x}) = [\boldsymbol{y}_{\mathrm{m}} - \boldsymbol{y}_{\mathrm{s}}(\boldsymbol{x})]^{\mathrm{T}} \cdot \mathbf{S}_{\epsilon}^{-1} \cdot [\boldsymbol{y}_{\mathrm{m}} - \boldsymbol{y}_{\mathrm{s}}(\boldsymbol{x})], \tag{6}$$

where $\mathbf{S}_{\epsilon}$ is the uncertainty covariance matrix. Assuming the measurements of each viewing elevation angle are independent, $\mathbf{S}_{\epsilon}$ is a diagonal matrix and its diagonal elements equal to the square of the measurement uncertainties of each elevation angle defined in Eq. (3),

$$\mathbf{S}_{\epsilon} = \begin{bmatrix} \epsilon_1^2 & 0 & \dots & 0 \\ 0 & \epsilon_2^2 & \dots & 0 \\ \vdots & \vdots & \ddots & \vdots \\ 0 & 0 & \dots & \epsilon_M^2 \end{bmatrix}. \tag{7}$$

Our cost function definition is similar to the cost functions used in many of the MAX-DOAS studies based on the OEM (e.g., Clémer et al., 2010; Frieß et al., 2016; Wang et al., 2016; Chan et al., 2017), but only includes the item related to measurement error, while the item related to the a priori profile is omitted. This is because the a priori profile is not needed in our retrieval algorithm.

χ^2 indicates the difference between $\boldsymbol{y}_{\mathrm{s}}$ and $\boldsymbol{y}_{\mathrm{m}}$, however, as the retrieval is ill-posed and the SNR of the measurement at the UFS is low, the single profile with the lowest χ^2 is not necessarily the one closest to the true profile. In order to overcome this limitation, we consider all the profiles in X_{LUT} with $\chi^2(\boldsymbol{x}) \leq 1.5M$ (9 in this study) as valid profiles and calculate the weighted mean profile as the optimal result. A profile with $\chi^2 \leq M$ indicates that the measured and simulated O_4 DSCDs agree within the measurement errors, but in order to avoid underestimation of the measurement errors, we defined the threshold as $1.5M$. The weight of each valid profile for the calculation of the optimal solution is defined as

$$w(\boldsymbol{x}) = \frac{1/\chi^2(\boldsymbol{x})}{\sum[1/\chi^2(\boldsymbol{x})]}, \boldsymbol{x} \in X_{\mathrm{LUT}}, \chi^2(\boldsymbol{x}) \leq 1.5M, \tag{8}$$

https://doi.org/10.5194/amt-2019-204
Preprint. Discussion started: 6 August 2019

Atmospheric Measurement Techniques Discussions

and the optimal solution can be calculated as

$$\hat{\boldsymbol{x}} = \sum w(\boldsymbol{x})\boldsymbol{x}, \boldsymbol{x} \in X_{\mathrm{LUT}}, \chi^2(\boldsymbol{x}) \leq 1.5M. \tag{9}$$

3.8 O_4 DSCD correction

Discrepancies between measured and simulated O_4 DSCDs are found in many other MAX-DOAS studies (Wagner et al., 2009; Clémer et al., 2010; Chan et al., 2015; Wang et al., 2016; Chan et al., 2017; Wagner et al., 2018). The discrepancies are often explained by the systematic error in the absorption cross section of O_4, and therefore correction is necessary. Previous studies suggested to multiply a constant scaling factor to the measured O_4 DSCD for all elevations to correct the systematic error (Wagner et al., 2009; Clémer et al., 2010; Chan et al., 2015; Wang et al., 2016). A recent study comparing modeled and measured (relative) intensity shows that the O_4 scaling factor might be dependent on the measurement elevation (Chan et al., 2017). In all these studies, simulated O_4 DSCDs were reported to be underestimated comparing to the measured ones.

In order to assess whether the O_4 correction is necessary for the MAX-DOAS measurement at the UFS, we compared the measured O_4 DSCDs to the simulated ones in the look-up table. Assuming our profile set (X_{LUT}) covers all the possible aerosol profiles under cloud-free condition, we derived the O_4 scaling factor for each elevation angle and each band based on the statistical analysis. The AODs measured by the sun photometer were used to restrict the range of possible profiles.

Fig. 4 shows the scattered plots of measured and simulated O_4 DSCDs of the scanning cycle on 07 Dec 2015 at ~13:55 UTC. Both the measurements of (a) UV and (b) VIS bands are shown. According to the cloud screening as well as the skycam images, this day was absolutely cloud free. Total AOD measured by the sun photometer at that time is 0.02 and 0.017 for 360 and 477 nm bands, respectively. The x-axis of the plots indicate the O_4 DSCDs measured (or simulated) at the elevation angle of 1°, while the y-axis represent the O_4 DSCDs measured (or simulated) at other elevation angles. Different colours indicate measurements at different elevation angles. The simulated O_4 DSCDs ($\boldsymbol{y}_{\mathrm{s}}(\boldsymbol{x})$) of all the possible profiles in X_{LUT} are shown as coloured dots. We assume the MAX-DOAS measurement of AOD between 0 and 2 km (denoted as $\tau_{2\mathrm{k}}$, $\tau_{2\mathrm{k}}(\boldsymbol{x}) = 0.5\sigma_1(\boldsymbol{x}) + 0.5\sigma_2(\boldsymbol{x}) + \sigma_3(\boldsymbol{x})$) varies between 50% and 100% of the total AOD measured by the sun photometer (denoted as $\tau_{\mathrm{sp},\lambda}$) in most cases, and the data points of the profiles fulfilling this assumption are highlighted. The measured O_4 DSCDs (already corrected for the systematic errors caused by the topography simplification) are plotted as square markers with error bars showing the total uncertainties. It is obvious that at most of the elevation angles, the measured O_4 DSCD does not agree with the simulations within the total error. As a result, at both UV and VIS bands, no profiles in X_{LUT} satisfy the selection requirement ($\chi^2 \leq 9$, see dashed curves in Fig. 5). No profiles matching the measurement is unlikely to happen under such clear sky condition, hence, implies a systematic error and correction of the error is necessary.

In order to determine whether the O_4 scaling factor is constant for all elevations or it is dependent on the viewing elevation angles, we plotted the variation range of the O_4 DSCD measurements in Fig. 4 assuming constant scaling factor for all elevation angles. The corrected O_4 DSCDs should vary along the coloured dashed lines if a constant scaling factor is applied to the measurements. The plus signs indicate the O_4 DSCDs corrected with constant scaling factors of 0.8, 0.9, 1.1 and 1.2,

https://doi.org/10.5194/amt-2019-204
Preprint. Discussion started: 6 August 2019

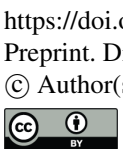

Atmospheric Measurement Techniques Discussions

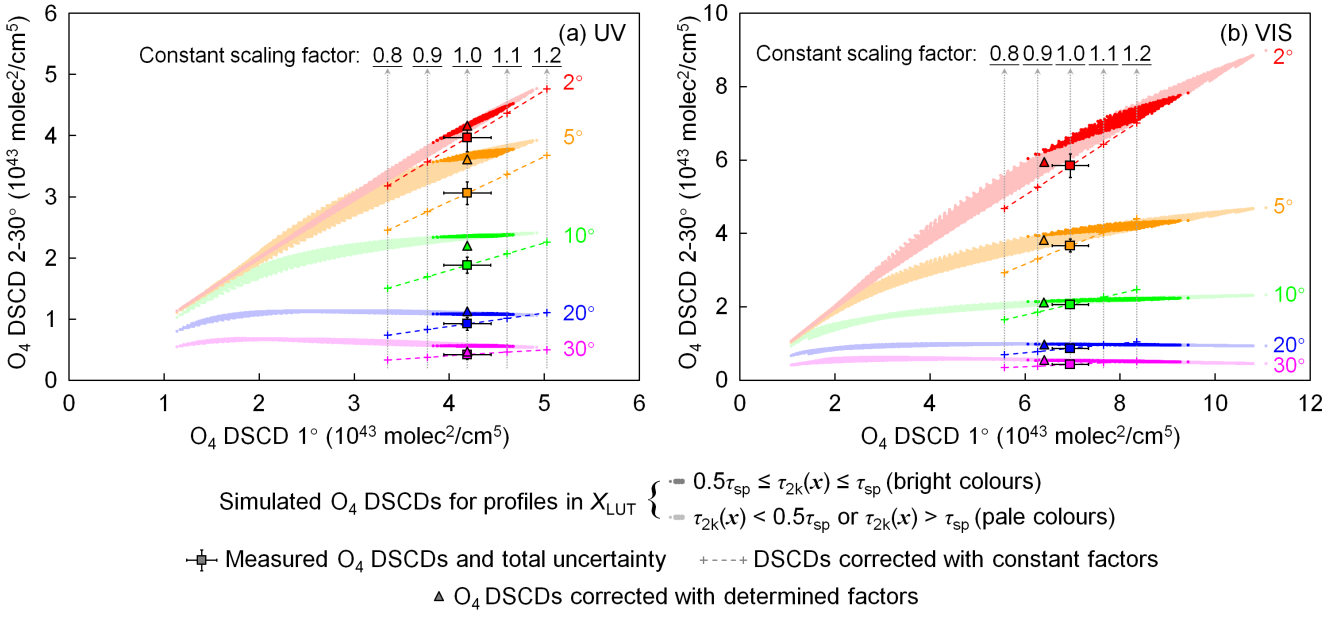

Figure 4. Distribution of simulated, measured and corrected O_4 DSCDs in (a) UV and (b) VIS bands of the scanning cycle on 07 Dec 2015 at ∼13:55 UTC. X-axis indicate the O_4 DSCDs measured (or simulated) at the elevation angle of 1°, while y-axis represent the O_4 DSCDs measured (or simulated) at other elevation angles. Different colours indicate measurements at different elevation angles. The coloured dots show the simulated O_4 DSCDs of all the possible profiles in the profile set (X_{LUT}). The dots of the profiles with AOD between 0 and 2 km ($\tau_{2\mathrm{k}}(\boldsymbol{x})$) varies between 50% and 100% of the total AOD measured by the sun photometer ($\tau_{\mathrm{sp},\lambda}$) are shown in bright colours, while the dots of the other profiles are shown in pale colours. The square markers represent measured O_4 DSCDs, and the error bars show the total uncertainties. Systematic errors caused by the topography simplification are already corrected from the measured O_4 DSCDs. The plus signs along the dashed lines show the measured O_4 DSCDs corrected with constant factors of 0.8, 0.9, 1.1 and 1.2. The triangle markers show the measured O_4 DSCDs corrected with the finally determined scaling factors listed in Table 4.

respectively. The forward simulation of O_4 DSCDs does not overlap with the dashed lines in most of the cases (especially for 5° and 10° of the UV band), indicating that a constant O_4 scaling factor for all viewing elevation angles could not resolve the systematic error. Therefore, different scaling factors should be applied to different elevation angles.

In this study, the O_4 DSCD scaling factors for each viewing elevation angle and wavelength were determined through the statistical analysis of the long-term observations. We assume the scaling factor mainly depends on the viewing elevation angle, while less sensitive to other factors, e.g., solar geometry and aerosol load.

Fig. 4 shows that the simulated O_4 DSCDs at high elevation angles (e.g. 20° and 30°) vary in a very narrow range. Based on the assumption that X_{LUT} covers all possible aerosol profiles, the measured O_4 DSCDs should lie within the range. The scaling factor can be derived by taking the ratio of the simulated and measured values. As the simulated value varies in a narrow range, the uncertainty of the derived scaling factor should also be low. In order to have a better statistic of the scaling factors, this

https://doi.org/10.5194/amt-2019-204
Preprint. Discussion started: 6 August 2019

Atmospheric Measurement Techniques Discussions

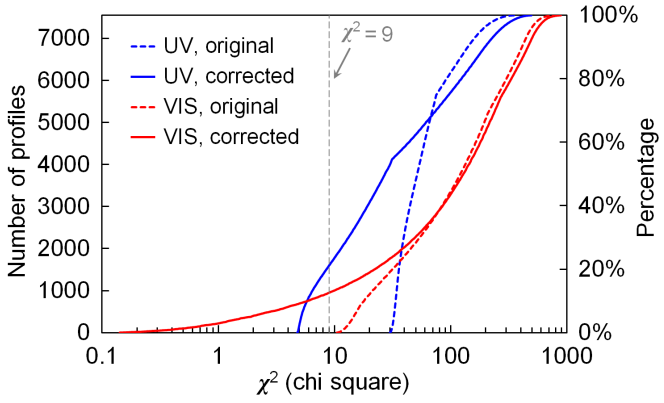

Figure 5. Cumulative distribution of the χ^2 of all the profiles in X_{LUT} for the scanning cycle at 07 Dec 2015 ~13:55 UTC. Dashed and solid curves refer to the results before and after the O_4 DSCD correction, respectively. Blue and red curves refer to the results of the UV and VIS bands, respectively. Note that the x-axis is logarithmically scaled.

method was applied to the long-term measurements. In addition, only the measurements taken under cloud-free and low aerosol load ($\tau_{\mathrm{sp},\lambda} \leq 0.03$) conditions were used, so as to avoid accounting data contaminated by clouds in the analysis. Here it should be noted that measurements with AOD < 0.03 are almost entirely found during winter. Subsequently, for the wavelength λ and the i^{th} elevation angle of each scanning cycle, we calculate the variation range of the simulated O_4 DSCDs for all the profiles fulfilling $0.5\tau_{\mathrm{sp},\lambda} \leq \tau_{2\mathrm{k}}(\boldsymbol{x}) \leq \tau_{\mathrm{sp},\lambda}$, which can be described as a set,

$$Y^*_{\lambda,i} = \{f(\boldsymbol{x}, \lambda, \alpha_i, \theta_i, \phi_i) \mid \boldsymbol{x} \in X_{\mathrm{LUT}}, 0.5\tau_{\mathrm{sp},\lambda} \leq \tau_{2\mathrm{k}}(\boldsymbol{x}) \leq \tau_{\mathrm{sp},\lambda}\}. \tag{10}$$

Only if $\max(Y^*_{\lambda,i}) \leq 1.1 \times \min(Y^*_{\lambda,i})$, then the scanning cycle was taken into account. In most cases, measured O_4 DSCDs at high elevation angles are lower than simulated ones, therefore we calculate the scaling factor from the minimum value in $Y^*_{\lambda,i}$ to avoid over-estimation of the scaling factor. The scaling factor derived from this scanning cycle is denoted as

$$\gamma^*_{\lambda,i} = \frac{\min(Y^*_{\lambda,i})}{\Delta S_{\lambda,i}}, \tag{11}$$

where $\Delta S_{\lambda,i}$ is the measured O_4 DSCD (already corrected for the systematic errors caused by the topography). For the elevation angles of 5°, 10°, 20°, 30° of UV band and 10°, 20°, 30° of VIS band, numerous scanning cycles from the long-term measurement fulfill the selection criterion, and hence there are sufficient samples of $\gamma^*_{\lambda,i}$ for statistical analysis. We analyzed the frequency distribution of $\gamma^*_{\lambda,1i}$ of each elevation and each wavelength band. The result shows that the distributions of $\gamma^*_{\lambda,1i}$ follow the normal distribution function with small standard deviation. For instance, for the elevation angle of 20°, the standard deviations of UV and VIS bands are both ~0.16. Subsequently, $\gamma^*_{\lambda,1i}$ with the maximum frequency was derived by Gaussian fit. The peak value is used as the scaling factor which is denoted as $\hat{\gamma}_{\lambda,i}$.

https://doi.org/10.5194/amt-2019-204
Preprint. Discussion started: 6 August 2019

Atmospheric Measurement Techniques Discussions

For the low elevation angles (1° and 2° of UV band, 1°, 2° and 5° of VIS band), as O_4 DSCD varies in a wide range, it is impossible to determine the scaling factor with the method mentioned above. However, it is found that in many scanning cycles, within the possible profiles in X_{LUT}, the simulated O_4 DSCDs at low elevation angles are well correlated to those at the neighbouring elevation angle. Therefore, once the scaling factor of the higher elevation angle is determined, we can derive an expected value of the O_4 DSCD at the lower elevation angle from the corrected O_4 DSCD at the higher elevation angle, and the scaling factor can be derived by taikng the ratio of the expected value and the measured value.

For the wavelength λ and for each scanning cycle, a subset of X_{LUT} is defined as

$$X^{\dagger} = \{\boldsymbol{x} \mid \boldsymbol{x} \in X_{\mathrm{LUT}}, 0 \leq \tau_{2\mathrm{k}}(\boldsymbol{x}) \leq 2\tau_{\mathrm{sp},\lambda}\}, \tag{12}$$

and the elements of $X^{\dagger}$ are denoted as $\boldsymbol{x}_j^{\dagger}$. The corresponding simulated O_4 DSCD at the i^{th} elevation angle is denoted as

$$\Delta S_{i,j}^{\dagger} = f(\boldsymbol{x}_j^{\dagger}, \lambda, \alpha_i, \theta_i, \phi_i), \boldsymbol{x}_j^{\dagger} \in X^{\dagger}. \tag{13}$$

A 3^{rd} order polynomial regression is applied between $\Delta S_{i,j}^{\dagger}$ and $\Delta S_{i+1,j}^{\dagger}$. The regression function is denoted as g. Only if the correlation coefficient $R^2 \geq 0.98$, this scanning cycle is taken into account. As the scaling factor of the $(i+1)^{\mathrm{th}}$ elevation ($\hat{\gamma}_{\lambda,i+1}$) is already determined, the expected value of the O_4 DSCD at the i^{th} elevation angle can be derived with the regression function:

$$E[\Delta S_{\lambda,i}] = g(\Delta S_{\lambda,i+1} \cdot \hat{\gamma}_{\lambda,i+1}), \tag{14}$$

and the scaling factor derived from this scanning cycle is

$$\gamma_{\lambda,i}^{\dagger} = \frac{E[\Delta S_{\lambda,i}]}{\Delta S_{\lambda,i}}. \tag{15}$$

Similar to the high elevation angles, the frequency distribution of $\gamma_{\lambda,i}^{\dagger}$ from all the available samples was analyzed by fitting to a Gaussian function. The peak $\gamma_{\lambda,i}^{\dagger}$ is used as $\hat{\gamma}_{\lambda,i}$. The scaling factor of the $(i-1)^{\mathrm{th}}$ elevation is then derived in the same way. The scaling factors of 1° and 2° of UV band and 1°, 2°, 5° of VIS band were determined using this method.

The determined scaling factors are listed in Table 4. The corrected O_4 DSCDs are indicated as triangles in Fig. 4. The result shows that except the elevation angle of 1°, the simulated O_4 DSCDs are overestimated comparing to the measured ones. It should be noted that the determination of the scaling factors is based on the measured O_4 DSCDs which are already corrected for the systematic errors caused by the topography simplification (discussed in 3.3). Comparing to the original measurements, the result still indicates that the simulated O_4 DSCDs at high elevation angles are overestimated. This result is opposite to the results of the other studies. The difference might be caused by the high altitude or the complex topography.

https://doi.org/10.5194/amt-2019-204
Preprint. Discussion started: 6 August 2019

Atmospheric Measurement Techniques Discussions

Table 4. The finally determined O_4 DSCD scaling factors.

Elevation angle	Factors for corrected O_4 DSCDs[(a)]		Factors for original O_4 DSCDs	
	UV (360 nm)	VIS (477 nm)	UV (360 nm)	VIS (477 nm)
1°	1.00	0.92	0.97	0.90
2°	1.05	1.02	1.01	1.00
5°	1.18	1.04	1.14	1.02
10°	1.17	1.03	1.12	0.99
20°	1.22	1.12	1.16	1.08
30°	1.12	1.27	1.06	1.22

[(a)] Means the O_4 DSCDs which are already corrected for the systematic errors caused by the topography simplification.

Fig. 5 shows the cumulative distribution of χ^2 of all the profiles in X_{LUT} for the scanning cycle shown in Fig. 4. The distribution of χ^2 before and after the DSCD correction are shown as dashed and solid curves, respectively. It can be seen that for both UV (blue curves) and VIS (red curves) bands, the χ^2 of most profiles in X_{LUT} are significantly lower after the correction. As a result, a number of profiles fulfill the selection criterion ($\chi^2 \leq 9$). Note that the AODs measured by MAX-DOAS are still expected to be lower than the sun photometer observations due to the fact that the MAX-DOAS only reports the AOD below 2 km while the sun photometer covers the entire atmosphere.

4 Results and discussion

Our retrieval algorithm was applied to the long-term measurement data of the UFS MAX-DOAS from February 2012 to February 2013 and from July 2013 to February 2016. The results are also compared to sun photometer measurement. This section presents the results as well as the discussion based on the results.

4.1 Dependency of retrieval result on the threshold of cost function

As presented in Section 3.7, we consider all the profiles with $\chi^2 \leq 9$ as valid profiles, and the retrieved profile is defined as the weighted mean of all the possible profiles. In this section, we investigate the dependency of the retrieval result on the threshold of χ^2 by comparing the results calculated with different different χ^2 thresholds. Take the scanning cycle on 07 Dec 2015 at ~13:55 UTC as an example, Fig. 6 shows the weighted mean profiles, the variation range of valid profiles and the number of valid profiles corresponding to different χ^2 thresholds. The profiles are shown as coloured curves which indicate the aerosol extinction coefficients in the three layers (i.e. σ_1, σ_2 and σ_3). The distribution of χ^2 of this scanning cycle is already shown as the solid curves in Fig. 5.

The result shows that the retrieved profile is not sensitive to the threshold of χ^2 when there are sufficient number of valid profiles (for UV, χ^2 threshold exceeds ~6 and number of profiles exceeds ~800, see the grey curve in Fig. 6 (a); for VIS, χ^2

https://doi.org/10.5194/amt-2019-204
Preprint. Discussion started: 6 August 2019

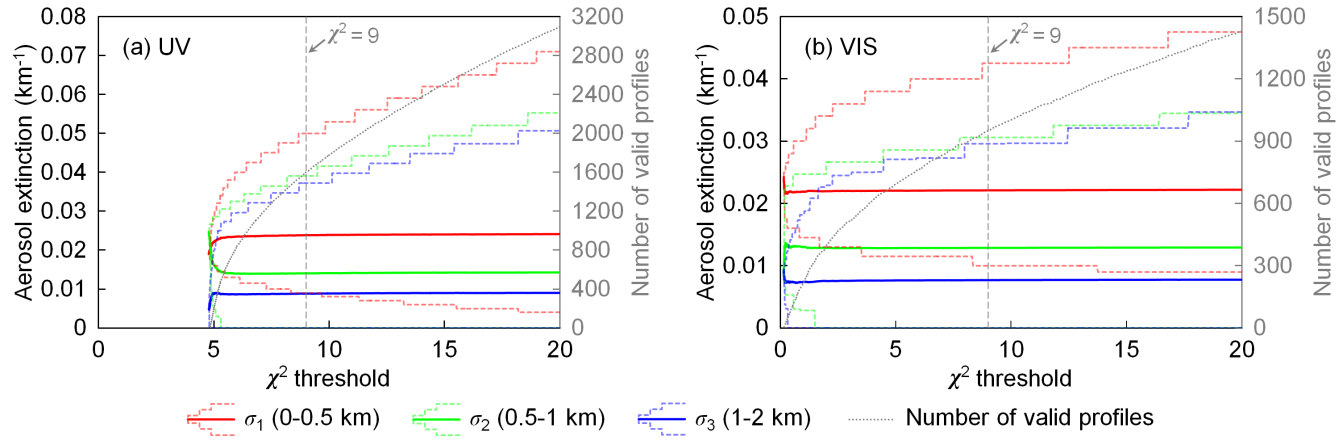

Figure 6. Weighted mean profiles, variation ranges of valid profiles and number of valid profiles of (a) UV and (b) VIS bands corresponding to different χ^2 thresholds, results of the scanning cycle on 07 Dec 2015 at ∼13:55 UTC. The weighted mean profiles are shown as solid curves which indicate the aerosol extinction coefficients in the three layers (σ_1, σ_2 and σ_3). The variation ranges of valid profiles are shown as dashed curves which indicates the variation ranges of σ_1, σ_2 and σ_3. The grey dotted curves indicate the number of valid profiles corresponding to different thresholds of χ^2. Measured O_4 DSCDs are corrected with the scaling factors listed in Table 4.

threshold exceeds ∼2 and number of profiles exceeds ∼400, see the grey curve in Fig. 6 (b)). This is because profiles with larger χ^2 have lower weight (w). In addition, when the threshold value is increased, more profiles with both higher and lower aerosol extinction coefficients are taken into account. As a result, the variation range of valid profiles becomes larger but the weighted mean remains similar. The result shows that the retrieval with a χ^2 threshold of 9 is stable, therefore, it is used in the study.

4.2 Estimation of the uncertainties of retrieved profiles

Still taking the scanning cycle on 07 Dec 2015 at ∼13:55 UTC as an example, we analyzed the weight distribution of valid profiles, see Fig. 7. The distributions of aerosol extinction coefficients in the three layers (σ_1, σ_2 and σ_3) are shown as solid curves. For each layer, aerosol extinction coefficients of all the valid profiles are grouped with a step size of 0.005 km^{-1}. The y-axis refers to the total weight of each group. The three vertical dashed lines indicate the weighted mean aerosol extinction coefficient of each layer (i.e. σ_1, σ_2 and σ_3 of $\hat{\boldsymbol{x}}$). The result shows that the distributions of σ_1, σ_2 and σ_3 are all asymmetric for both the UV and VIS bands. Especially for the layer of 1 – 2 km (σ_3), the weight decreases monotonically with increasing aerosol extinction. At UV band, there are altogether 205 valid profiles with $\sigma_3 = 0$, which contribute a total weight of 0.122. At VIS band, there are altogether 120 valid profiles with $\sigma_3 = 0$, which contribute a total weight of 0.101.

In order to estimate the uncertainty of $\hat{\boldsymbol{x}}$, we calculate the weighted standard deviations of σ_1, σ_2 and σ_3 of all the valid profiles. Due to the asymmetric distribution, the weighted standard deviations are calculated separately for both left (negative)

https://doi.org/10.5194/amt-2019-204
Preprint. Discussion started: 6 August 2019

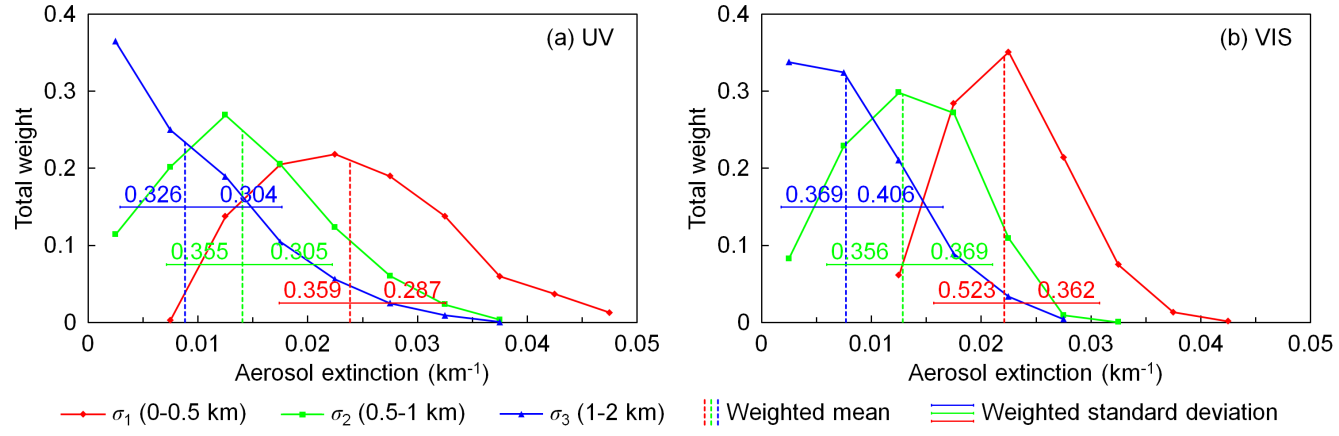

Figure 7. Weight distribution of valid profiles of (a) UV and (b) VIS bands, results of the scanning cycle on 07 Dec 2015 at ∼13:55 UTC. The weight distributions of the aerosol extinction coefficients of the three layers (σ_1, σ_2 and σ_3) are shown as solid curves with different colours, for bins of 0.005 km^{-1}. The vertical dashed lines indicate the weighted mean aerosol extinction coefficient of the three layers ($\sigma_1(\hat{\boldsymbol{x}})$, $\sigma_2(\hat{\boldsymbol{x}})$ and $\sigma_3(\hat{\boldsymbol{x}})$). The error bars indicate the weighted standard deviation calculated with Eq. (16) and (17). The numbers on the error bars refer to the total weight (w) of the profiles covered by each error bar.

and right (positive) sides. For the l^{th} ($l = 1,2,3$) layer, denote the aerosol extinction coefficient of each profile as $\sigma_l(\boldsymbol{x})$, the weighted standard deviation of the left side is calculated from all the valid profiles with $\sigma_l(\boldsymbol{x}) < \sigma_l(\hat{\boldsymbol{x}})$,

$$SD_l^- = \sqrt{\frac{\sum w(\boldsymbol{x}) \cdot [\sigma_l(\hat{\boldsymbol{x}}) - \sigma_l(\boldsymbol{x})]^2}{\sum w(\boldsymbol{x})}}, \boldsymbol{x} \in X_{\text{LUT}}, \chi^2(\boldsymbol{x}) \leq 1.5M, \sigma_l(\boldsymbol{x}) < \sigma_l(\hat{\boldsymbol{x}}), \tag{16}$$

and the weighted standard deviation of the right side is calculated from all the valid profiles with $\sigma_l(\boldsymbol{x}) > \sigma_l(\hat{\boldsymbol{x}})$,

$$SD_l^+ = \sqrt{\frac{\sum w(\boldsymbol{x}) \cdot [\sigma_l(\boldsymbol{x}) - \sigma_l(\hat{\boldsymbol{x}})]^2}{\sum w(\boldsymbol{x})}}, \boldsymbol{x} \in X_{\text{LUT}}, \chi^2(\boldsymbol{x}) \leq 1.5M, \sigma_l(\boldsymbol{x}) > \sigma_l(\hat{\boldsymbol{x}}), \tag{17}$$

The uncertainties of $\hat{\boldsymbol{x}}$ are indicated as error bars in Fig. 7. For each layer, the total weight of the profiles covered by the error bar is labeled in Fig. 7. At the UV band, the total weight of the valid profiles covered by the uncertainties is 63 – 66% which is close to the standard normal distribution. At the VIS band, the percentage is 78 – 90%. This is because the SNR of the measurement at the VIS band is higher. Therefore the retrieval of VIS band has higher selectivity, and the weight is more concentrated to the mean value.

4.3 Retrieval of synthetic measurement data

In order to test our retrieval algorithm, we generated some synthetic measurement data and retrieved with our algorithm. Fig. 8 shows the result of an artificial profile with a tangent like shape. The aerosol profile used to generate the syntheic O_4 DSCDs

https://doi.org/10.5194/amt-2019-204
Preprint. Discussion started: 6 August 2019

Atmospheric Measurement Techniques Discussions

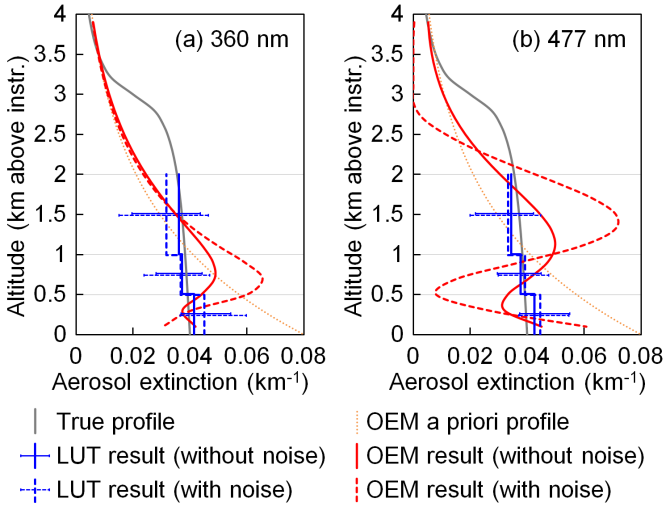

Figure 8. Retrieval results of synthetic data for (a) 360 and (b) 477 nm. The gray curves show the true profile, with which the synthetic O_4 DSCDs were simulated. The blue and red curves represent the profiles retrieved using our LUT (look-up table) algorithm and a typical OEM (optimal estimation method) algorithm, respectively. The sold blue and red curves represent the profiles retrieved from the original synthetic data, and the dashed curves represent the profiles retrieved from the synthetic data with random noised added. The error bars of the blue curves indicate the uncertainties calculated by Eq. (16) and (17). The dotted orange curves are the a priori profile used in the OEM retrieval.

is shown as the gray curves in Fig. 8. Aerosols are distributed between 0 and 6 km above instrument with total AOD of 0.12. The aerosol extinction coefficient decreases with increasing altitude. The aerosol extinction coefficient at surface is 0.04 km^{-1}. The aerosol extinction coefficient reduces to ~96% of the surface layer at 1 km above instrument, ~89% at 2 km, 50% at 3 km, and 0 at 6 km. As the aerosol extinction coefficient decreases slowly at low altitudes, ~92% of the total AOD is contributed from the altitude below 3 km. According to the long-term measurements of the co-located sun photometer and ceilometer, this profile is representative for the UFS.

We first simulated O_4 DSCDs at 360 and 477 nm using the profile with SZA of 60° and RAA of 60°. The solid blue curves in Fig. 8 show the profiles retrieved with our algorithm under noise free condition, and the error bars indicate the uncertainties calculated by Eq. (16) and (17). In order to test the stability of the retrieval, we have also added a random noise to the simulated O_4 DSCDs. We assume the measurement noise of all elevation angles are the same which follow a normal distribution with the standard deviation of 2% of the DSCD of the lowest elevation angle. This noise level is realistic for the measurements at the UFS. The profiles retrieved from the noisy data are shown as dashed blue curves in Fig. 8. At both 360 and 477 nm, the retrieved profiles can well reproduce the true profile. Our LUT based retrieval is considered to be stable, as the results are very similar for both cases with and without noise.

We also retrieved the synthetic data with and without noise using a typical OEM profile retrieval algorithm. An exponential profile with AOD of 0.12 and scaling height of 1.5 km was used as the a priori profile in the OEM retrieval which is shown

https://doi.org/10.5194/amt-2019-204
Preprint. Discussion started: 6 August 2019

Atmospheric Measurement Techniques Discussions

in Fig. 8 as the dotted orange curve. The results retrieved from the data with and without noise are shown in Fig. 8 as solid and dashed red curves, respectively. For the noise-free case, the profiles retrieved with the OEM algorithm are unrealistic and aerosol extinction varies in a large range between adjacent layers. In addition, the profiles cannot reproduce the true profile. The OEM retrieval is also unstable, as not only the aerosol extinction but also the shape of the profile is significantly distorted when noise is added to the synthetic data. The result indicates that the LUT based algorithm is much more reliable and suitable for high altitude measurements.

4.4 Comparison to sun photometer measurement

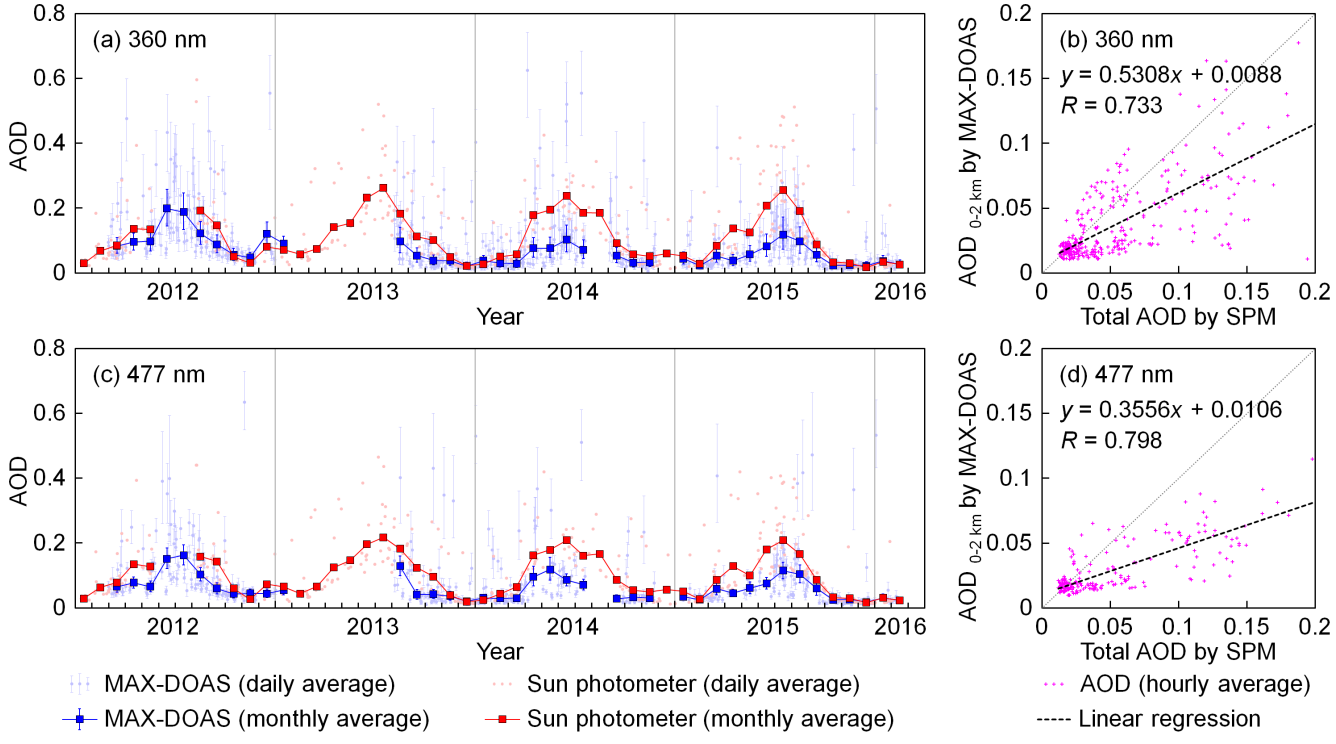

Figure 9. Comparison of AODs at (a, b) 360 nm and (c, d) 477 nm measured by MAX-DOAS and sun photometer. The charts on the left side (a, c) show the daily and monthly averaged time series, and the scatter plots on the right side (b, d) show the hourly averaged results. The AODs measured by MAX-DOAS refer to the AODs between 0 and 2 km above instrument (i.e. 2,650 – 4,650 m a.s.l.), and the meausrements were available during the daytime with SZA < 85° and no cloud; the AODs meausured by sun photometer refer to the total AOD, and the measurements were only available during 10:00 – 14:00 UTC. The daily and monthly averaged results are calculated from all the available hourly averaged AODs, therefore they are not real monthly and daily averages. The error bars of the MAX-DOAS data refer to the averages of the uncertainties calculated by Eq. (16) and (17). A few data points are outside the scatter plots.

https://doi.org/10.5194/amt-2019-204
Preprint. Discussion started: 6 August 2019

Atmospheric Measurement Techniques Discussions

Fig. 9 shows the comparison of AOD measured by MAX-DOAS and sun photometer during the entire study period. The seasonal average AOD measured by both instruments are listed in Table 5. The AOD measured by MAX-DOAS refers to the AOD between 0 and 2 km (i.e. $\tau_{2k}(\hat{\boldsymbol{x}}) = 0.5\sigma_1(\hat{\boldsymbol{x}}) + 0.5\sigma_2(\hat{\boldsymbol{x}}) + \sigma_3(\hat{\boldsymbol{x}})$), while the AOD measured by the sun photometer refers to the total AOD. Therefore, AODs measured by the sun photometer should be larger than AODs measured by the MAX-DOAS. Despite of the difference, the time series (panels a and c of Fig. 9) show that the AODs measured by both instruments have a similar seasonal variation with higher AOD in summer and lower AOD in winter.

Table 5. Seasonally averaged AODs measured by the MAX-DOAS and sun photometer at the UFS. The AODs measured by MAX-DOAS refer to the AODs between 0 and 2 km above instrument (i.e. 2,650 – 4,650 m a.s.l.), and the meausrements were available during the daytime with SZA < 85° and no cloud; the AODs meausred by sun photometer refer to the total AOD, and the measurements were only available during 10:00 – 14:00 UTC. The results listed in the table are calculated from all the available hourly averaged AODs.

Season	AOD (0 – 2 km) measured by MAX-DOAS		Total AOD measured by sun photometer	
	360 nm	477 nm	360 nm	477 nm
Spring (MAM)	0.064	0.065	0.106	0.101
Summer (JJA)	0.121	0.114	0.214	0.184
Autumn (SON)	0.048	0.040	0.070	0.068
Winter (DJF)	0.028	0.024	0.037	0.033

The correlation between hourly averaged AODs measured by MAX-DOAS and sun photometer is shown in Fig. 9 (b, d). AODs measured by MAX-DOAS show a general agreement with sun photometer measurements at both UV and VIS bands with correlation coefficients of $R = 0.733$ and 0.798, respectively. However, AODs from MAX-DOAS are lower, consequently the slope of the regression lines are 0.5308 and 0.3556 for UV and VIS bands, respectively. As the MAX-DOAS only reports AODs below 2 km while the sun photometer measures the total AODs, the MAX-DOAS AODs are indeed expected to be lower. This is in particular true in cases of large AODs due to very strong convection of polluted air masses from the valley and/or the presence of Saharan dust layers. Then, particles are often transported beyond the range of the MAX-DOAS measurements and the disagreement is largest. This feature might be strengthened by the decreased sensitivity of the MAX-DOAS measurement at higher altitudes, so that the upper part of an aerosol layer is missed. In addition, a few data points lie above the 1:1 reference lines, which indicates that the AODs measured by MAX-DOAS were occasionally higher than the sun photometer measurements. This might be explained by the inhomogeneous distribution of aerosols in horizontal direction. The light paths of MAX-DOAS and sun photometer are different. MAX-DOAS measures scattered sunlight while sun photometer derives AODs from direct sun measurements. Therefore, when the aerosol load along the light path of MAX-DOAS is higher than that of the direct sun measurement, the AOD measured by the MAX-DOAS may exceed the AOD measured by the sun photometer. Moreover, for most of these points, the difference between the results of the two instruments is within the uncertainty of the MAX-DOAS result defined by Eq. (16), therefore some of these points are probably due to the measurement error.

https://doi.org/10.5194/amt-2019-204
Preprint. Discussion started: 6 August 2019

Atmospheric Measurement Techniques Discussions

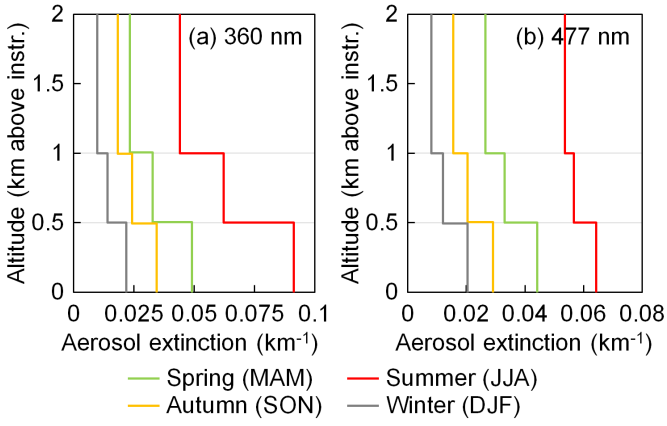

Figure 10. Seasonal average aerosol extinction profiles for (a) 360 and (b) 477 nm derived from the long-term measurement results. The altitude refers to the altitude above instrument.

4.5 Temporal variation characteristic of aerosols

The seasonally averaged aerosol extinction profiles derived from the long-term measurements are shown in Fig. 10. The result indicates that the aerosol load is high in summer and low in winter. This can be explained by the higher biogenic emissions from vegetation in summer. Moreover, the mixing layer is higher in summer, thus anthropogenic aerosols are more likely dispersed to upper altitudes. The result also shows that the aerosol extinction decreases with increasing altitude in all seasons – taking into account the coarse vertical resolution.

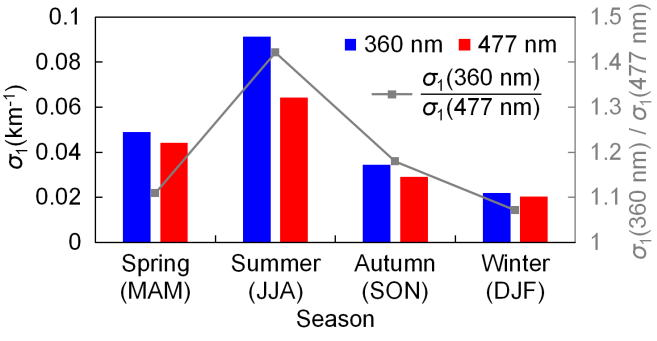

Figure 11. Comparison of seasonal average aerosol extinction coefficients at 360 and 477 nm in the bottom layer (0 – 0.5 km above instrument, σ_1). The coloured bars show the average aerosol extinction coefficients of the four seasons (equal to the bottom values shown in Fig. 10). The grey square markers indicate the ratios between the aerosol extinction coefficients at 360 and 477 nm.

https://doi.org/10.5194/amt-2019-204
Preprint. Discussion started: 6 August 2019

Atmospheric Measurement Techniques Discussions

We compared the seasonal average aerosol extinction coefficients at 360 and 477 nm in the bottom layer (0 – 0.5 km above instrument, σ_1), see Fig. 11. The averaged aerosol extinction coefficients are shown as bar charts. The ratio between the aerosol extinction coefficients at 360 and 477 nm is indicated by the grey curve. The result shows that the aerosol extinction coefficient ratio between 360 and 477 nm is significantly higher in summer than in the other seasons.

From these ratios the Ångström exponents (AEs) can easily be calculated using the seasonally averaged surface aerosol extinction coefficients at 360 and 477 nm. The results are listed in Table 6. The seasonal averaged AEs of 380 – 500 nm from the AERONET measurements at Hohenpeißenberg from Apr 2013 to Feb 2016 are listed for comparison. The result shows that both the UFS and Hohenpeißenberg measured the highest AE in summer and the lowest in winter. The AE at the UFS is in general lower than that measured at Hohenpeißenberg with a smaller difference in summer. This can be explained by the different altitude of the two sites. As the AERONET station at Hohenpeißenberg is located at ∼950 m a.s.l., larger contribution of anthropogenic aerosols is expected. The extremely low AE at the UFS in spring, autumn and winter agrees with the result measured at a plateau site (Lhasa, China, 3,688 m a.s.l.) reported in Xin et al. (2007). The annual mean AE at that site is reported to be 0.06 ± 0.31, which is significantly lower than those measured at low-altitude sites, especially urban and forest sites. In general, smaller AEs imply larger aerosol particle sizes (Dubovik et al., 2002). The increased AE at UFS in summer indicates that the particle size is smaller in summer and implies larger contribution of fine particles being transported from the lower altitudes to upper altitudes.

Table 6. Seasonal average Ångström exponents (AEs) obtained from MAX-DOAS near-surface measurements (0 – 0.5 km above instrument) and from AERONET measurements at Hohenpeißenberg. The results of MAX-DOAS are calculated from the ratios between the seasonal average aerosol extinction coefficients at 360 and 477 nm (i.e. the ratios shown in Fig. 11). The results of AERONET are the seasonal average values of AEs (380 – 500 nm) at Hohenpeißenberg from Apr 2013 to Feb 2016.

Season	AE from UFS MAX-DOAS	AE from AERONET at Hohenpeißenberg
Spring (MAM)	0.37	1.26
Summer (JJA)	1.25	1.38
Autumn (SON)	0.59	1.05
Winter (DJF)	0.24	0.47

5 Summary and conclusions

We have developed a new aerosol profile retrieval algorithm for MAX-DOAS measurements at high altitude sites. This is challenging as the AODs are typically quite low. The algorithm is based on a parameterized O_4 DSCD look-up table. The algorithm is applied to the long-term MAX-DOAS measurement at the UFS, located at an altitude of 2,650 m a.s.l. Aerosol measurements from February 2012 to February 2016 are considered.

Observations of O_4 absorption at both 360 and 477 nm are analyzed. Due to the low SNR, commonly used MAX-DOAS retrieval algorithms based on the optimal estimation method are not suitable for the retrieval of high altitude measurements.

https://doi.org/10.5194/amt-2019-204
Preprint. Discussion started: 6 August 2019

Atmospheric Measurement Techniques Discussions

In order to better design the O_4 DSCD look-up table, we investigated the sensitivities of O_4 absorption to ground topography, surface albedo, single scattering albedo, scattering phase function, aerosols at different altitude and surface aerosol extinction. The O_4 DSCD look-up table was then parameterized based on the results of the sensitivity study. According to the sensitivity analysis result, we defined a set of possible aerosol extinction profiles and simulated the O_4 DSCDs with all the possible profiles and observation geometries. In the retrieval of each measurement cycle, the simulated O_4 DSCDs corresponding to all the possible profile are obtained from the look-up. The cost functions (χ^2) are calculated for each possible profile according to the simulated and measured O_4 DSCDs as well as the measurement uncertainties. A comprehensive error analysis was performed to better estimate the total uncertainty. The errors from DOAS fitting, temperature, ground topography simplification, ground surface albedo, single scattering albedo, phase function and aerosols above retrieval height are considered. Valid profiles are selected from the profile set according to the cost function. The optimal solution is defined as the weighted mean of the valid profiles. Our analysis shows that the weighted mean profile is almost insensitive to the threshold of χ^2. The uncertainty of the solution is defined as the weighted standard deviation of the valid profiles.

One key result of our study is that an elevation dependent O_4 DSCD scaling factor is needed to bring measurements and model results into agreement. Assuming the look-up table covers all the possible aerosol profiles under clear sky conditions, we determined the scaling factors based on the statistical analysis of the long-term measurement. At the moment we have no clear explanation for this finding, it might be related to the specific properties of the high altitude station, e.g. the highly structured topography, horizontal gradients of the aerosol extinction and the systematic dependence of the surface albedo on altitude. The agreement between measured and simulated O_4 DSCDs is greatly improved by the correction.

In addition, we developed a simple cloud screening method which is based on the statistical analysis of the colour index. The developed cloud screening method is applied to the long-term measurement to filter out data taken under cloudy conditions.

In order to demonstrate the reliablility and stability of the algorithm, we have tested the algorithm with syntheic data. The results indicate that our algorithm can well reproduce the true profile, and the retrieval is stable for the retrieval of aerosol profile at hight altitude site. The AODs retrieved from the long-term MAX-DOAS measurements using our developed inversion technique are compared to the sun photometer observations at the UFS. The results show reasonable agreement with each other with correlation coefficients (R) of 0.733 and 0.798 for measurements at UV and VIS bands, respectively. However, especially in summer the sun photometer results are systematically larger (by about a factor of 2) than the MAX-DOAS results. This discrepancy is due to the different definition of AODs measured by MAX-DOAS and sun photometer, and also probably related to the decreased sensitivity of the MAX-DOAS measurements at higher altitudes. It becomes relevant in cases of large AODs when Saharan dust was present or strong convection occurred. The long-term observation results show that the aerosol load at the UFS is higher in summer and lower in winter. Higher AOD in summer is mainly related to a higher frequency of extended mixing layers that allows anthropogenic pollutants to disperse from lower to upper altitudes. According to the MAX-DOAS measurements the aerosol extinction decreases with increasing altitude for all seasons. The Angström exponent is higher in summer and extremely low in winter, which implies a smaller particle size in summer. This might be due to a significant contribution from biogenic sources in summer.

https://doi.org/10.5194/amt-2019-204
Preprint. Discussion started: 6 August 2019

Atmospheric Measurement Techniques Discussions

The study demonstrated that the developed method is effective for MAX-DOAS measurements at the UFS. Since the profile set only consists of reasonable profiles, and the final solutions are calculated from the weighted means of all the valid profiles, as well as the retrieval does not rely on a priori profiles, many of the limitations of the retrieval algorithms based on the optimal estimation method are overcome. In addition, as the O_4 DSCDs of all the possible profiles are pre-calculated, our method significantly reduces the computational time, so that real-time retrieval is possible.

Appendix A: Cloud screening method

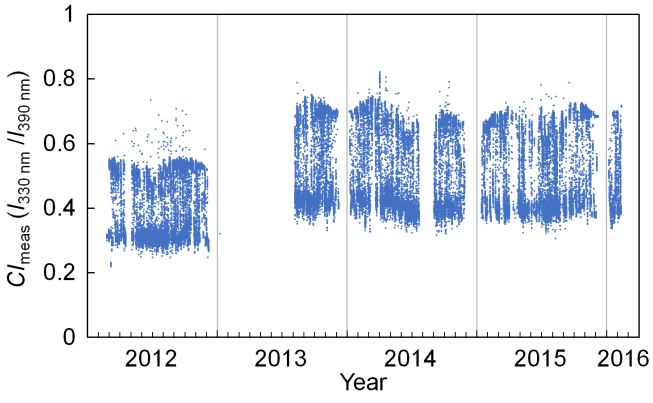

Figure A1. Time series of CI_{meas} calculated from the zenith UV spectra measured during the entire study with 30° < SZA < 70°.

In this study, the colour index (CI) is defined as the ratio of radiative intensities at 330 and 390 nm. Measured CIs (denoted as CI_{meas}) were calculated from the zenith UV spectra (offset and dark current corrected) by taking the ratio of the counts at 330 and 390 nm. Fig. A1 shows the time sereies of CI_{meas} calculated from all the zenith spectra with 30° < SZA (solar zenith angle) < 70° during the entire study. The result shows that the variation range of CI_{meas} is stable within the two periods. However, the optical throughput of the instrument in the UV spectral range has been enhanced after a regular maintenance of the optical system in 2013. Hence, the CI increased systematically in the second period. Therefore, calibration of CI_{meas} is necessary in order to make the CI_{meas} measured during the two periods comparable to each other. The calibration was done following the method suggested in Wagner et al. (2016). CI_{meas} measured under overcast skies were fitted to the simulated minimum CI. The correction factor was determined to be 2.70 and 2.06 for the periods of 02.2012 – 01.2013 and 08.2013 – 02.2016, respectively. CI_{meas} was subsequently converted to CI_{cal} (calibrated CI) by multiplying the corresponding correction factor.

Fig. A2 shows the frequency distribution of CI_{cal} measured with different SZAs. The CI_{cal} from the long-term measurement were grouped by their SZA with a step size of 2°. The relative frequency distributions are colour coded. The result shows a bimodal frequency distribution of CI_{cal} for all SZAs. The peaks with lower and higher CI are corresponding to measurements under overcast and clear skies, respectively. This pattern is similar to the CI measured on Jungfraujoch, Switzerland (3570 m

https://doi.org/10.5194/amt-2019-204
Preprint. Discussion started: 6 August 2019

Atmospheric Measurement Techniques Discussions

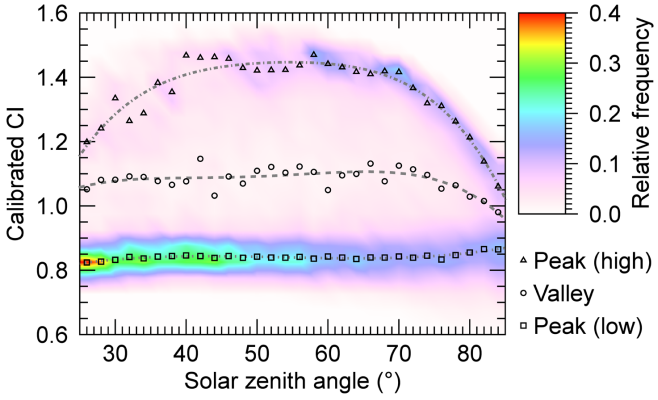

Figure A2. Distribution pattern of CI_{cal} during the entire study. Data were grouped by SZA with an interval of 2°. For each group, frequency was counted for bins of 0.05. Peak and valley values (shown as markers) were determined by Gaussian fit. The curves are the results of 4$^{\text{th}}$ order polynomial regressions of each data series.

a.s.l.) reported in Gielen et al. (2014), and different from the results measured at the low-altitude sites reported in Gielen et al. (2014); Wagner et al. (2016). This is because the high altitude sites are seldom influenced by anthropogenic aerosols, hence the sky is either clear or covered by cloud or fog during most of the time. Based on this feature, we defined the threshold for cloud screening as the CI_{cal} with the minimum probability between the two peaks (denoted as $CI_{\text{cal, valley}}$). The $CI_{\text{cal, valley}}$ was determined by fitting the probability density function to a Gaussian function. The circle markers shown in Fig. A2 indicates the determined $CI_{\text{cal, valley}}$. In order to minimize the noise, the $CI_{\text{cal, valley}}$ was fitted to a 4$^{\text{th}}$ order polynomial. The resulting smoothed $CI_{\text{cal, valley}}$ was used as the threshold (indicated as dashed curve in Fig. A2). Based on this approach, ~60% of the zenith measurements were determined as cloudy scenes, and the corresponding scanning cycles were not used in the following analysis.

Appendix B: Result of the sensitivity studies

We investigated the sensitivity of O_4 absorption to surface albedo, single scattering albedo, scattering phase function, aerosol extinction at different altitude, aerosol extinction above retrieval height, and surface aerosol extinction. In the test for each parameter, O_4 DSCDs at the six off-zenith elevations were simulated with all other parameters fixed to their median values. In all the simulations, the surface was defined as a flat surface at an altitude of 2,650 m a.s.l. (see Section 3.3). All the examples shown in this section were simulated with the solar position set as SZA = 60° and RAA = 60°, which are close to the median values of SZA and RAA at the UFS during daytime. Since the sensitivities can be influenced by the measurement geometry, the error estimation in the retrieval is based on error look-up tables which cover all the possible combinations of measurement geometry. In this section, all the altitudes mentioned hereinafter refer to the relative altitude above the instrument.

https://doi.org/10.5194/amt-2019-204
Preprint. Discussion started: 6 August 2019

Atmospheric Measurement Techniques Discussions

B1 Sensitivity to surface albedo

It is difficult to estimate the surface albedo around the measurement site. In other studies, the surface albedo at low altitude sites was usually estimated to be 0.05 – 0.1 (e.g., Irie et al., 2008; Ma et al., 2013; Wagner et al., 2011; Chan et al., 2017; Li et al., 2010; Clémer et al., 2010; Li et al., 2013; Wang et al., 2016), while at a high altitude site, it was estimated to be 0.2 (Franco et al., 2015). As for the UFS, on one hand, the snow covers and naked rocks are more reflective than the typical urban and rural surfaces; on the other hand, the deep valleys close to the site can significantly decrease the surface albedo. In addition, the measurements at different elevation angles are sensitive to different parts of surface. The effective surface albedo also depends on the observation geometry. The forming and melting of the snow cover can affect the surface albedo as well. However, the RTM can only assume a constant surface albedo. Therefore, we have to estimate a variation range of the surface albedo and consider the possible uncertainty in the retrieval. In this study, we empirically estimate that the surface albedo varies between 0.025 and 0.2 with a median value of 0.1 for both 360 and 477 nm.

O_4 DSCDs at 360 and 477 nm were simulated with extreme surface albedo values (0.025 and 0.2) and the median value (0.1). Simulations were done with both an aerosol-free profile and a box-shape profile with AOD = 0.12 and box height = 3 km. Fig. B1 shows the relative differences of the O_4 DSCDs simulated with extreme surface albedo values compared to those simulated with the median value in the both studies.

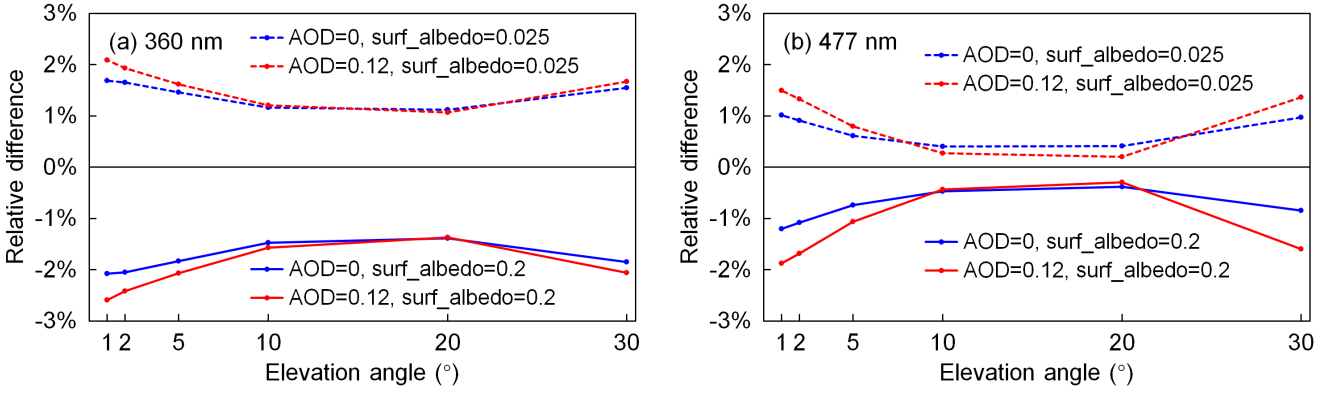

Figure B1. Relative differences of O_4 DSCDs at (a) 360 nm and (b) 477 nm simulated with extreme surface albedo values (solid lines for 0.2 and dashed lines for 0.025) compared to O_4 DSCDs simulated with the median value (0.1). Blue lines refer to the results under aerosol-free condition, while red lines refer to the results with a box-shape profile with AOD = 0.12 and box height = 3 km. The solar position was set as SZA = 60° and RAA = 60°.

The result shows that at both 360 and 477 nm, O_4 DSCDs of all the elevation angles slightly decrease with increasing surface albedo, and the variation rate differs with different elevation angle and different aerosol load. Based on our estimation of the variation range of surface albedo, if the estimated median value (0.1) is used in the forward simulation, the uncertainty caused by the surface albedo assumption would be less than 3%, and the positive and negative errors are nearly equal. Our further

https://doi.org/10.5194/amt-2019-204
Preprint. Discussion started: 6 August 2019

Atmospheric Measurement Techniques Discussions

simulations also show that the uncertainty caused by albedo depends on the observation geometry. In the following simulations hereafter, the surface albedo was set to 0.1 unless otherwise mentioned.

B2 Sensitivity to single scattering albedo

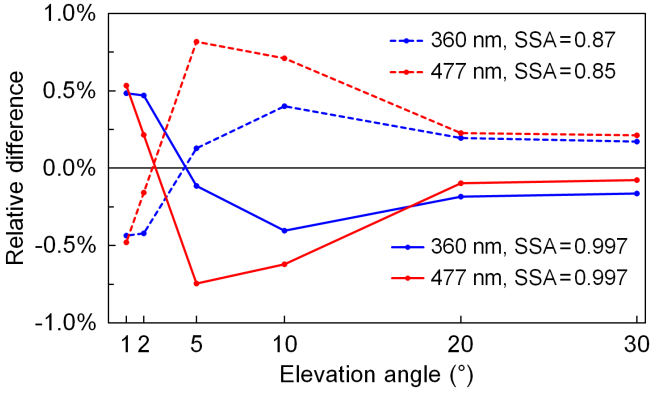

Figure B2. Relative differences of O_4 DSCDs at 360 nm (blue lines) and 477 nm (red lines) simulated with extreme single scattering albedo values (solid lines for larger extreme value and dashed lines for smaller extreme value) compared to O_4 DSCDs simulated with the median value (0.93 for 360 nm and 0.92 for 477 nm). The solar position was set as SZA = 60° and RAA = 60°.

As aerosol optical property data at the UFS are not available, and we use the AERONET data at Hohenpeißenberg instead. According to the long-term data, for the single scattering albedo (SSA) at 360 nm, 90% of the data vary between 0.87 and 0.997, and the median value is 0.93; for the SSA at 477 nm, 90% of the data vary between 0.85 and 0.997, and the median value is 0.92.

O_4 DSCDs at 360 and 477 nm were simulated with the median and extreme SSA values (0.87, 0.93 and 0.997 for 360 nm; 0.85, 09.2 and 0.997 for 477 nm). In all the simulations, aerosol profile was defined as a box-shape profile with AOD = 0.12 and box height = 3 km. The relative differences between the O_4 DSCDs simulated with extreme and median SSA values are shown in Fig. B2.

The result indicates that using the median SSA in the forward simulation would result in less than 1% error in O_4 DSCDs in 90% of the cases. In addition, the positive and negative errors are mostly equal. Although the measurement of SSA are taken from a much lower altitude site, the sensitivity result shows the error attributed to SSA is rather small (<1%). Therefore, using the SSA values from Hohenpeißenberg should not have a big influence on the retrieval. From hereafter, all radiative transfer simulations assume SSA of 0.93 for 360 nm and 0.92 for 477 nm unless otherwise mentioned.

https://doi.org/10.5194/amt-2019-204
Preprint. Discussion started: 6 August 2019

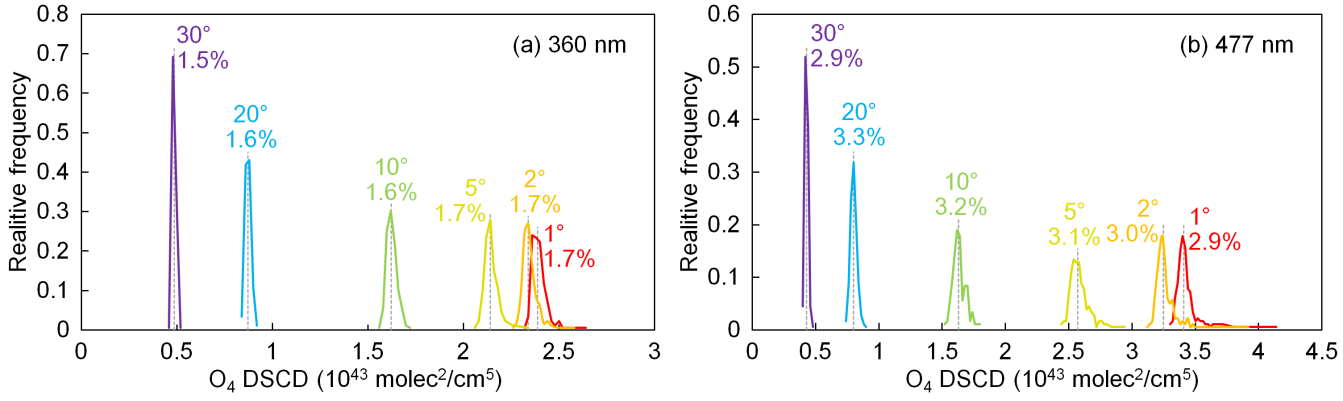

Figure B3. Frequency distribution of O_4 DSCDs at (a) 360 nm and (b) 477 nm simulated with all the phase functions during 2013 – 2014. The aerosol profile was set as a box-shape profile with AOD = 0.12 and box height = 3 km. The solar position was set as SZA = 60° and RAA = 60°. The percentage standard deviations of the simulated O_4 DSCDs at each elevation angle are labeled in the plots. The grey dashed lines represent the median values of simulated O_4 DSCDs at each elevation angle.

B3 Sensitivity to scattering phase function

The sensitivity of O_4 DSCDs to scattering phase function was estimated by using all the phase functions measured by the AERONET station from 2013 to 2014 in the forward simulation of O_4 DSCDs with a fixed aerosol profile (a box-shape profile with AOD = 0.12 and box height = 3 km). The frequency distributions of simulated O_4 DSCDs at all elevation angles are shown in Fig. B3. The percentage standard deviations of the results are also indicated. The median values of the simulated O_4 DSCDs at each elevation angle are shown as grey dashed lines. The results show that the distributions of the simulated O_4 DSCDs at all elevation angles follow the normal distribution, and the simulation uncertainty caused by phase function is larger than that caused by SSA. Similar to the SSA sensitivity analysis, using phase functions from Hohenpeißenberg should not have a significant impact on the aerosol retrieval. Hereafter, the phase function with simulated O_4 DSCDs at all elevation angles closest to the median values are used in the forward simulation, and this phase function is denoted as the 'median' phase function.

B4 Sensitivity to aerosols at different altitude

The sensitivity of O_4 DSCD to aerosol extinction at different altitude was estimated by simulating O_4 DSCDs with box-shape aerosol profiles with the same aerosol extinction coefficient of 0.04 km^{-1} and different box heights varying from 0 to 8 km. Fig. B4 shows the simulated O_4 DSCDs at 360 and 477 nm for each elevation angle. The result indicates that the sensitivities of O_4 DSCDs at all elevation angles decrease rapidly with increasing box height (and also increasing AOD). Furthermore, O_4 DSCDs at all elevation angles are almost constant when the box height varies between 2 and 8 km, which indicates that O_4 absorption is almost insensitive to the aerosols above 2 km. Take the O_4 DSCD measured at 360 nm with elevation angle of 2°

https://doi.org/10.5194/amt-2019-204
Preprint. Discussion started: 6 August 2019

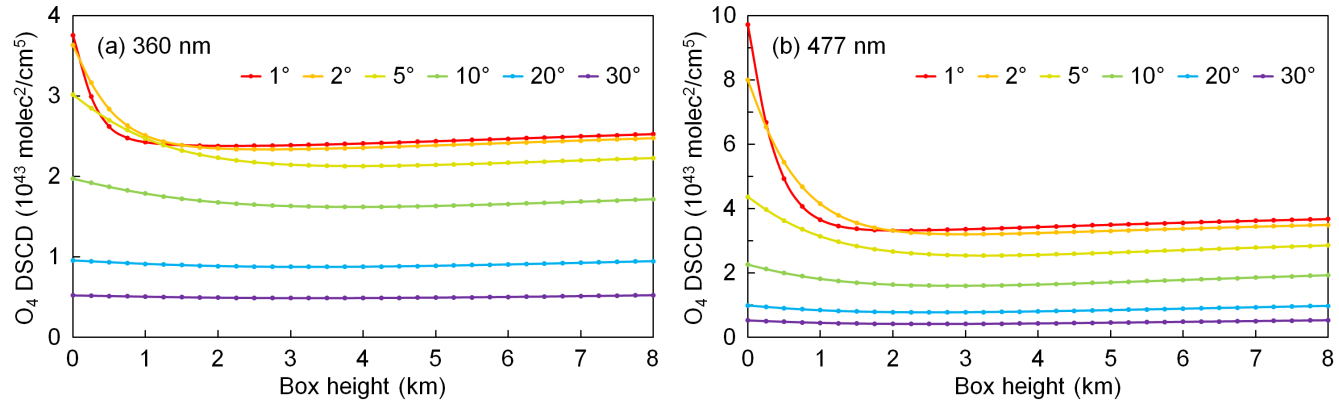

Figure B4. Simulated O_4 DSCDs at (a) 360 nm and (b) 477 nm for box-shape profiles with the same surface aerosol extinction coefficient of 0.04 km^{-1} and different box heights from 0 to 8 km. The solar position was set as SZA = 60° and RAA = 60°.

as an example, the sensitivity to aerosols at 2 km is lower than that at surface level by a factor of ∼40. In addition, measurements at lower elevation angles are more sensitive to aerosols close to the surface compared to higher elevations. According to the result, our retrieval of aerosol profiles would only focus on aerosols below 2 km.

The result is consistent with the results reported in the previous OEM based MAX-DOAS studies (e.g., Frieß et al., 2006; Clémer et al., 2010; Frieß et al., 2016; Bösch et al., 2018). In these studies, the averaging kernels — which indicate the measurement sensitivity to aerosols at different altitude — are all close to zero at the altitudes above 2 km.

B5 Sensitivity to aerosols above retrieval height

As discussed in Section B4, our aerosol profile retrieval would only focus on aerosols below 2 km. However, as the aerosol load on Zugspitze is usually very low and the aerosol extinction coefficient above 2 km is usually in the same order of magnitude with the one below 2 km. We estimate that the aerosol extinction coefficient between 2 and 4 km (denote as AE_{2-4}) varies from 0% to 100% of the aerosol below 2 km (denote as AE_{0-2}), and the median value is 50% of AE_{0-2}. In order to estimate the sensitivity of O_4 absorption to AE_{2-4}, O_4 DSCDs were simulated with profiles with the same aerosol extinction coefficient below 2 km (AE_{0-2} = 0.04 km^{-1}) and AE_{2-4} equals to 0%, 50% and 100% of AE_{0-2}. The differences between the O_4 DSCDs simulated with extreme and median AE_{2-4} are shown in Fig. B5. The result indicates that the aerosols above 2 km can affect the O_4 DSCDs by up to ∼3%, which is similar to the surface albedo. Therefore, we consider the influence from the aerosols above 2 km as a kind of measurement uncertainty, and treat it in the same way as the errors caused by surface albedo, single scattering albedo and phase function uncertainties.

https://doi.org/10.5194/amt-2019-204
Preprint. Discussion started: 6 August 2019

Atmospheric Measurement Techniques Discussions

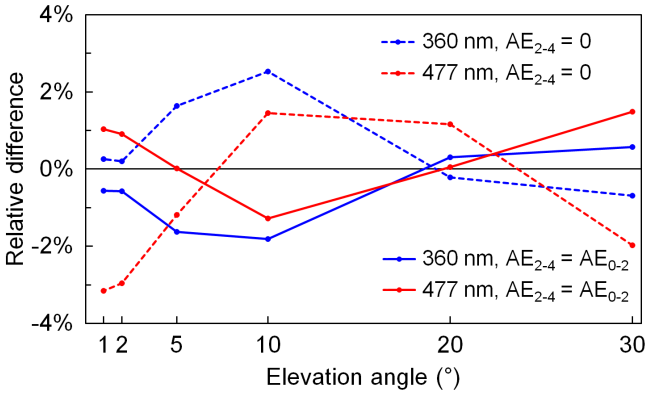

Figure B5. Relative differences of O_4 DSCDs at 360 nm (blue lines) and 477 nm (red lines) simulated with aerosol profiles with AE_{2-4} (aerosol extinction coefficient between 2 and 4 km above instrument) equals to 0% (dashed lines) and 100% (solid lines) of AE_{0-2} (aerosol extinction coefficient between 0 and 2 km above instrument) comparing to the O_4 DSCDs simulated with a profile with $AE_{2-4} = 50\% AE_{0-2}$. For all the profiles, $AE_{0-2} = 0.04\ km^{-1}$. The solar position was set as SZA = 60° and RAA = 60°.

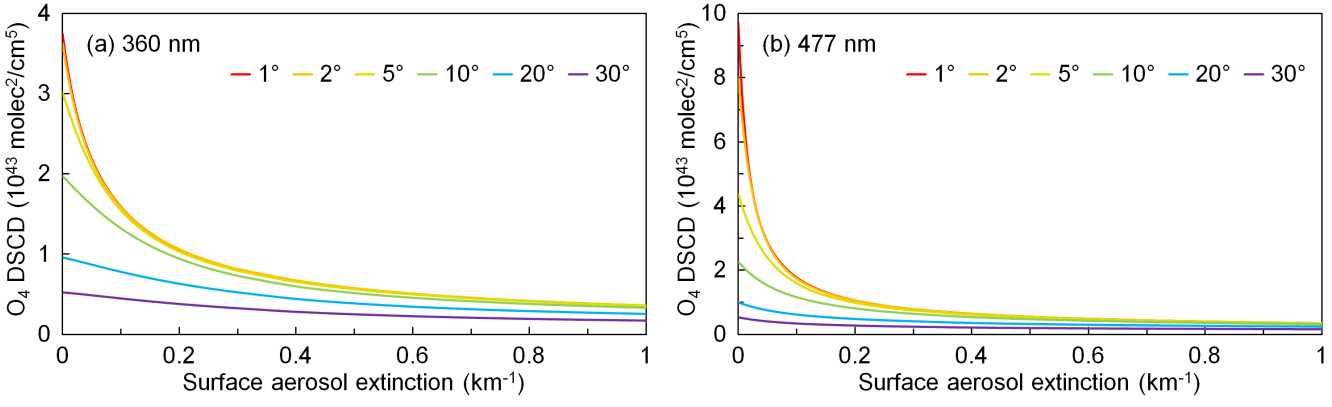

Figure B6. Simulated O_4 DSCDs at (a) 360 nm and (b) 477 nm for box-shape profiles with the same box height of 2 km and different surface aerosol extinction coefficients from 0 to 1 km^{-1}. The solar position was set as SZA = 60° and RAA = 60°. Note that the curves of 1° and 2° are quite close to each other.

B6 Sensitivity to surface aerosol extinction

The sensitivity of O_4 DSCD to surface aerosol extinction was estimated by forward radiative transfer simulation with box aerosol profiles. The aerosol profiles were parameterized with constant box height of 2 km and aerosol extinction coefficient varies from 0 to 1 km^{-1}. The other simulation settings were the same as those incicated in Section B4. Fig. B6 shows the simulated O_4 DSCDs for each elevation angle and both (a) 360 nm and (b) 477 nm. The result shows that the sensitivities of

https://doi.org/10.5194/amt-2019-204
Preprint. Discussion started: 6 August 2019

Atmospheric Measurement Techniques Discussions

O_4 absorption at all elevation angles and both wavelength bands decrease with increasing aerosol extinction. Furthermore, the sensitivity is very low when the surface aerosol extinction coefficient exceeds 0.3 km^{-1}. The O_4 DSCDs at all elevation angles and both wavelengths decrease monotonically with increasing aerosol extinction. In addition, measurements at lower elevation angles are much more sensitive.

Competing interests. The authors declare that they have no conflict of interest.

Acknowledgements. This work is funded by the DLR-DAAD Research Fellowships 2014 (50019750) programme with reference number 91549461. We are thankful for the help from the colleagues of University of Heidelberg in installing the MAX-DOAS instrument at the UFS. We thank Ina Mattis and her colleagues at DWD for their effort in establishing and maintaining the AERONET site in Hohenpeißenberg. The authors would also like to thank the Royal Belgian Institute for Space Aeronomy (BIRA-IASB) for the provision of the QDOAS software used in this study. We are grateful to Till Rehm and his colleagues at the UFS for the maintenance work. We thank the Bayrisches Umweltminsterium for supporting the UFS as part of their mission.

https://doi.org/10.5194/amt-2019-204
Preprint. Discussion started: 6 August 2019

Atmospheric Measurement Techniques Discussions

References

Aliwell, S. R., Roozendael, M. V., Johnston, P. V., Richter, A., Wagner, T., Arlander, D. W., Burrows, J. P., Fish, D. J., Jones, R. L., Tørnkvist, K. K., Lambert, J.-C., Pfeilsticker, K., and Pundt, I.: Analysis for BrO in zenith-sky spectra: An intercomparison exercise for analysis improvement, Journal of Geophysical Research: Atmospheres, 107, ACH 10–1–ACH 10–20, https://doi.org/10.1029/2001JD000329, 2002.

Almeida-Silva, M., Almeida, S. M., Freitas, M. C., Pio, C. A., Nunes, T., and Cardoso, J.: Impact of Sahara Dust Transport on Cape Verde Atmospheric Element Particles, Journal of Toxicology and Environmental Health, Part A, 76, 240–251, https://doi.org/10.1080/15287394.2013.757200, 2013.

Bäumer, D., Vogel, B., Versick, S., Rinke, R., Möhler, O., and Schnaiter, M.: Relationship of visibility, aerosol optical thickness and aerosol size distribution in an ageing air mass over South-West Germany, Atmospheric Environment, 42, 989 – 998, https://doi.org/https://doi.org/10.1016/j.atmosenv.2007.10.017, http://www.sciencedirect.com/science/article/pii/S1352231007008977, 2008.

Bellouin, N., Boucher, O., Haywood, J., and Reddy, M. S.: Global estimate of aerosol direct radiative forcing from satellite measurements, Nature, 438, 1138–1141, https://doi.org/doi:10.1038/nature04348, 2005.

Bogumil, K., Orphal, J., Homann, T., Voigt, S., Spietz, P., Fleischmann, O., Vogel, A., Hartmann, M., Kromminga, H., Bovensmann, H., Frerick, J., and Burrows, J.: Measurements of molecular absorption spectra with the SCIAMACHY pre-flight model: instrument characterization and reference data for atmospheric remote-sensing in the 230-2380 nm region, Journal of Photochemistry and Photobiology A: Chemistry, 157, 167–184, https://doi.org/http://dx.doi.org/10.1016/S1010-6030(03)00062-5, atmospheric Photochemistry, 2003.

Bösch, T., Rozanov, V., Richter, A., Peters, E., Rozanov, A., Wittrock, F., Merlaud, A., Lampel, J., Schmitt, S., de Haij, M., Berkhout, S., Henzing, B., Apituley, A., den Hoed, M., Vonk, J., Tiefengraber, M., Müller, M., and Burrows, J. P.: BOREAS – a new MAX-DOAS profile retrieval algorithm for aerosols and trace gases, Atmospheric Measurement Techniques, 11, 6833–6859, https://doi.org/10.5194/amt-11-6833-2018, https://www.atmos-meas-tech.net/11/6833/2018/, 2018.

Brook, R. D., Rajagopalan, S., Pope, C. A., Brook, J. R., Bhatnagar, A., Diez-Roux, A. V., Holguin, F., Hong, Y., Luepker, R. V., Mittleman, M. A., Peters, A., Siscovick, D., Smith, S. C., Whitsel, L., and Kaufman, J. D.: Particulate Matter Air Pollution and Cardiovascular Disease, Circulation, 121, 2331–2378, https://doi.org/10.1161/CIR.0b013e3181dbece1, 2010.

Cazorla, A., Casquero-Vera, J. A., Román, R., Guerrero-Rascado, J. L., Toledano, C., Cachorro, V. E., Orza, J. A. G., Cancillo, M. L., Serrano, A., Titos, G., Pandolfi, M., Alastuey, A., Hanrieder, N., and Alados-Arboledas, L.: Near-real-time processing of a ceilometer network assisted with sun-photometer data: monitoring a dust outbreak
over the Iberian Peninsula, Atmospheric Chemistry and Physics, 17, 11 861–11 876, https://doi.org/10.5194/acp-17-11861-2017, https://www.atmos-chem-phys.net/17/11861/2017/, 2017.

Chan, K., Wiegner, M., Wenig, M., and Pöhler, D.: Observations of tropospheric aerosols and NO_2 in Hong Kong over 5 years using ground based MAX-DOAS, Science of The Total Environment, https://doi.org/https://doi.org/10.1016/j.scitotenv.2017.10.153, 2017.

Chan, K. L.: Biomass burning sources and their contributions to the local air quality in Hong Kong, Science of The Total Environment, 596-597, 212–221, https://doi.org/https://doi.org/10.1016/j.scitotenv.2017.04.091, 2017.

Chan, K. L. and Chan, K. L.: Aerosol optical depths and their contributing sources in Taiwan, Atmospheric Environment, 148, 364–375, https://doi.org/http://dx.doi.org/10.1016/j.atmosenv.2016.11.011, 2017.

https://doi.org/10.5194/amt-2019-204
Preprint. Discussion started: 6 August 2019

Chan, K. L., Hartl, A., Lam, Y. F., Xie, P. H., Liu, W. Q., Cheung, H. M., Lampel, J., Pöhler, D., Li, A., Xu, J., Zhou, H. J., Ning, Z., and Wenig, M. O.: Observations of tropospheric NO_2 using ground based MAX-DOAS and OMI measurements during the Shanghai World Expo 2010, Atmospheric Environment, 119, 45–58, https://doi.org/http://dx.doi.org/10.1016/j.atmosenv.2015.08.041, 2015.

Chan, K. L., Wiegner, M., Flentje, H., Mattis, I., Wagner, F., Gasteiger, J., and Geiß, A.: Evaluation of ECMWF-IFS (version 41R1) operational model forecasts of aerosol transport by using ceilometer network measurements, Geoscientific Model Development, 11, 3807–3831, https://doi.org/10.5194/gmd-11-3807-2018, 2018.

Chance, K. and Kurucz, R.: An improved high-resolution solar reference spectrum for earth's atmosphere measurements in the ultraviolet, visible, and near infrared, Journal of Quantitative Spectroscopy and Radiative Transfer, 111, 1289 – 1295, https://doi.org/https://doi.org/10.1016/j.jqsrt.2010.01.036, 2010.

Chance, K. and Orphal, J.: Revised ultraviolet absorption cross sections of H2CO for the HITRAN database, Journal of Quantitative Spectroscopy and Radiative Transfer, 112, 1509 – 1510, https://doi.org/https://doi.org/10.1016/j.jqsrt.2011.02.002, 2011.

Chance, K. V. and Spurr, R. J. D.: Ring effect studies: Rayleigh scattering, including molecular parameters for rotational Raman scattering, and the Fraunhofer spectrum, Appl. Opt., 36, 5224–5230, https://doi.org/10.1364/AO.36.005224, http://ao.osa.org/abstract.cfm?URI=ao-36-21-5224, 1997.

Clémer, K., Van Roozendael, M., Fayt, C., Hendrick, F., Hermans, C., Pinardi, G., Spurr, R., Wang, P., and De Mazière, M.: Multiple wavelength retrieval of tropospheric aerosol optical properties from MAXDOAS measurements in Beijing, Atmospheric Measurement Techniques, 3, 863–878, https://doi.org/10.5194/amt-3-863-2010, 2010.

Deutschmann, T.: Atmospheric radiative transfer modelling with Monte Carlo methods, Institute of environmental physics University of Heidelberg, p. 3935, 2008.

Dubovik, O., Holben, B., Eck, T. F., Smirnov, A., Kaufman, Y. J., King, M. D., Tanré, D., and Slutsker, I.: Variability of Absorption and Optical Properties of Key Aerosol Types Observed in Worldwide Locations, Journal of the Atmospheric Sciences, 59, 590–608, https://doi.org/10.1175/1520-0469(2002)059<0590:VOAAOP>2.0.CO;2, 2002.

Franco, B., Hendrick, F., Van Roozendael, M., Müller, J.-F., Stavrakou, T., Marais, E. A., Bovy, B., Bader, W., Fayt, C., Hermans, C., Lejeune, B., Pinardi, G., Servais, C., and Mahieu, E.: Retrievals of formaldehyde from ground-based FTIR and MAX-DOAS observations at the Jungfraujoch station and comparisons with GEOS-Chem and IMAGES model simulations, Atmospheric Measurement Techniques, 8, 1733–1756, https://doi.org/10.5194/amt-8-1733-2015, https://www.atmos-meas-tech.net/8/1733/2015/, 2015.

Frieß, U., Monks, P. S., Remedios, J. J., Rozanov, A., Sinreich, R., Wagner, T., and Platt, U.: MAX-DOAS O_4 measurements: A new technique to derive information on atmospheric aerosols: 2. Modeling studies, Journal of Geophysical Research: Atmospheres, 111, https://doi.org/10.1029/2005JD006618, 2006.

Frieß, U., Sihler, H., Sander, R., Pöhler, D., Yilmaz, S., and Platt, U.: The vertical distribution of BrO and aerosols in the Arctic: Measurements by active and passive differential optical absorption spectroscopy, Journal of Geophysical Research: Atmospheres, 116, https://doi.org/10.1029/2011JD015938, https://agupubs.onlinelibrary.wiley.com/doi/abs/10.1029/2011JD015938, 2011.

Frieß, U., Klein Baltink, H., Beirle, S., Clémer, K., Hendrick, F., Henzing, B., Irie, H., de Leeuw, G., Li, A., Moerman, M. M., van Roozendael, M., Shaiganfar, R., Wagner, T., Wang, Y., Xie, P., Yilmaz, S., and Zieger, P.: Intercomparison of aerosol extinction profiles retrieved from MAX-DOAS measurements, Atmospheric Measurement Techniques, 9, 3205–3222, https://doi.org/10.5194/amt-9-3205-2016, https://www.atmos-meas-tech.net/9/3205/2016/, 2016.

https://doi.org/10.5194/amt-2019-204
Preprint. Discussion started: 6 August 2019

Atmospheric Measurement Techniques Discussions

Gielen, C., Van Roozendael, M., Hendrick, F., Pinardi, G., Vlemmix, T., De Bock, V., De Backer, H., Fayt, C., Hermans, C., Gillotay, D., and Wang, P.: A simple and versatile cloud-screening method for MAX-DOAS retrievals, Atmospheric Measurement Techniques, 7, 3509–3527, https://doi.org/10.5194/amt-7-3509-2014, 2014.

Halla, J. D., Wagner, T., Beirle, S., Brook, J. R., Hayden, K. L., O'Brien, J. M., Ng, A., Majonis, D., Wenig, M. O., and McLaren, R.: Determination of tropospheric vertical columns of NO_2 and aerosol optical properties in a rural setting using MAX-DOAS, Atmospheric Chemistry and Physics, 11, 12 475–12 498, https://doi.org/10.5194/acp-11-12475-2011, 2011.

Hartl, A. and Wenig, M. O.: Regularisation model study for the least-squares retrieval of aerosol extinction time series from UV/VIS MAX-DOAS observations for a ground layer profile parameterisation, Atmospheric Measurement Techniques, 6, 1959–1980, https://doi.org/10.5194/amt-6-1959-2013, 2013.

Haywood, J. and Boucher, O.: Estimates of the direct and indirect radiative forcing due to tropospheric aerosols: A review, Reviews of Geophysics, 38, 513–543, https://doi.org/10.1029/1999RG000078, 2000.

Heald, C. L., Ridley, D. A., Kroll, J. H., Barrett, S. R. H., Cady-Pereira, K. E., Alvarado, M. J., and Holmes, C. D.: Contrasting the direct radiative effect and direct radiative forcing of aerosols, Atmospheric Chemistry and Physics, 14, 5513–5527, https://doi.org/10.5194/acp-14-5513-2014, 2014.

Hinds, W. C.: Aerosol technology: properties, behavior, and measurement of airborne particles, John Wiley & Sons, 2012.

Holben, B., Eck, T., Slutsker, I., Tanre, D., Buis, J., Setzer, A., Vermote, E., Reagan, J., Kaufman, Y., Nakajima, T., Lavenu, F., Jankowiak, I., and Smirnov, A.: AERONET - A Federated Instrument Network and Data Archive for Aerosol Characterization, Remote Sensing of Environment, 66, 1–16, https://doi.org/http://dx.doi.org/10.1016/S0034-4257(98)00031-5, 1998.

Hönninger, G., von Friedeburg, C., and Platt, U.: Multi axis differential optical absorption spectroscopy (MAX-DOAS), Atmospheric Chemistry and Physics, 4, 231–254, https://doi.org/10.5194/acp-4-231-2004, 2004.

Irie, H., Kanaya, Y., Akimoto, H., Iwabuchi, H., Shimizu, A., and Aoki, K.: First retrieval of tropospheric aerosol profiles using MAX-DOAS and comparison with lidar and sky radiometer measurements, Atmospheric Chemistry and Physics, 8, 341–350, https://doi.org/10.5194/acp-8-341-2008, 2008.

Irie, H., Takashima, H., Kanaya, Y., Boersma, K. F., Gast, L., Wittrock, F., Brunner, D., Zhou, Y., and Van Roozendael, M.: Eight-component retrievals from ground-based MAX-DOAS observations, Atmospheric Measurement Techniques, 4, 1027–1044, https://doi.org/10.5194/amt-4-1027-2011, https://www.atmos-meas-tech.net/4/1027/2011/, 2011.

Jin, J., Ma, J., Lin, W., Zhao, H., Shaiganfar, R., Beirle, S., and Wagner, T.: MAX-DOAS measurements and satellite validation of tropospheric NO_2 and SO_2 vertical column densities at a rural site of North China, Atmospheric Environment, 133, 12–25, https://doi.org/http://dx.doi.org/10.1016/j.atmosenv.2016.03.031, 2016.

Junker, C. and Liousse, C.: A global emission inventory of carbonaceous aerosol from historic records of fossil fuel and biofuel consumption for the period 1860–1997, Atmospheric Chemistry and Physics, 8, 1195–1207, https://doi.org/10.5194/acp-8-1195-2008, https://www.atmos-chem-phys.net/8/1195/2008/, 2008.

Karanasiou, A., Moreno, N., Moreno, T., Viana, M., de Leeuw, F., and Querol, X.: Health effects from Sahara dust episodes in Europe: Literature review and research gaps, Environment International, 47, 107 – 114, https://doi.org/https://doi.org/10.1016/j.envint.2012.06.012, http://www.sciencedirect.com/science/article/pii/S0160412012001390, 2012.

Lee, H., Irie, H., Kim, Y. J., Noh, Y., Lee, C., Kim, Y., and Chun, K. J.: Retrieval of Aerosol Extinction in the Lower Troposphere Based on UV MAX-DOAS Measurements, Aerosol Science and Technology, 43, 502–509, https://doi.org/10.1080/02786820902769691, https://doi.org/10.1080/02786820902769691, 2009.

https://doi.org/10.5194/amt-2019-204
Preprint. Discussion started: 6 August 2019

Lee, Y. C., Lam, Y. F., Kuhlmann, G., Wenig, M. O., Chan, K. L., Hartl, A., and Ning, Z.: An integrated approach to identify the biomass burning sources contributing to black carbon episodes in Hong Kong, Atmospheric Environment, 80, 478–487, https://doi.org/http://dx.doi.org/10.1016/j.atmosenv.2013.08.030, 2013.

Levy II, H., Horowitz, L. W., Schwarzkopf, M. D., Ming, Y., Golaz, J.-C., Naik, V., and Ramaswamy, V.: The roles of aerosol direct and indirect effects in past and future climate change, Journal of Geophysical Research: Atmospheres, 118, 4521–4532, https://doi.org/10.1002/jgrd.50192, https://agupubs.onlinelibrary.wiley.com/doi/abs/10.1002/jgrd.50192, 2013.

Li, X., Brauers, T., Shao, M., Garland, R. M., Wagner, T., Deutschmann, T., and Wahner, A.: MAX-DOAS measurements in southern China: retrieval of aerosol extinctions and validation using ground-based in-situ data, Atmospheric Chemistry and Physics, 10, 2079–2089, https://doi.org/10.5194/acp-10-2079-2010, 2010.

Li, X., Brauers, T., Hofzumahaus, A., Lu, K., Li, Y. P., Shao, M., Wagner, T., and Wahner, A.: MAX-DOAS measurements of NO_2, HCHO and CHOCHO at a rural site in Southern China, Atmospheric Chemistry and Physics, 13, 2133–2151, https://doi.org/10.5194/acp-13-2133-2013, 2013.

Li, Z. and Kou, L.: The direct radiative effect of smoke aerosols on atmospheric absorption of visible sunlight, Tellus B, 50, 2011.

Liu, S. C., McKeen, S. A., and Madronich, S.: Effect of anthropogenic aerosols on biologically active ultraviolet radiation, Geophysical Research Letters, 18, 2265–2268, https://doi.org/10.1029/91GL02773, https://agupubs.onlinelibrary.wiley.com/doi/abs/10.1029/91GL02773, 1991.

Ma, J. Z., Beirle, S., Jin, J. L., Shaiganfar, R., Yan, P., and Wagner, T.: Tropospheric NO_2 vertical column densities over Beijing: results of the first three years of ground-based MAX-DOAS measurements (2008-2011) and satellite validation, Atmospheric Chemistry and Physics, 13, 1547–1567, https://doi.org/10.5194/acp-13-1547-2013, 2013.

Pappalardo, G., Amodeo, A., Apituley, A., Comeron, A., Freudenthaler, V., Linné, H., Ansmann, A., Bösenberg, J., D'Amico, G., Mattis, I., Mona, L., Wandinger, U., Amiridis, V., Alados-Arboledas, L., Nicolae, D., and Wiegner, M.: EARLINET: towards an advanced sustainable European aerosol lidar network, Atmospheric Measurement Techniques, 7, 2389–2409, https://doi.org/10.5194/amt-7-2389-2014, https://www.atmos-meas-tech.net/7/2389/2014/, 2014.

Platt, U. and Stutz, J.: Differential optical absorption spectroscopy - principles and applications, Springer, 2008.

Platt, U., Perner, D., and Patz, H. W.: Simultaneous measurement of atmospheric CH_2O, O_3, and NO_2 by differential optical absorption, Journal of Geophysical Research: Oceans, 84, 6329–6335, https://doi.org/10.1029/JC084iC10p06329, 1979.

Risius, S., Xu, H., Di Lorenzo, F., Xi, H., Siebert, H., Shaw, R. A., and Bodenschatz, E.: Schneefernerhaus as a mountain research station for clouds and turbulence, Atmospheric Measurement Techniques, 8, 3209–3218, https://doi.org/10.5194/amt-8-3209-2015, 2015.

Rodgers, C. D.: Inverse methods for atmospheric sounding: Theory and practice, vol. 2, World scientific, 2000.

Rothman, L., Gordon, I., Barber, R., Dothe, H., Gamache, R., Goldman, A., Perevalov, V., Tashkun, S., and Tennyson, J.: HITEMP, the high-temperature molecular spectroscopic database, Journal of Quantitative Spectroscopy and Radiative Transfer, 111, 2139 – 2150, https://doi.org/https://doi.org/10.1016/j.jqsrt.2010.05.001, 2010.

Serdyuchenko, A., Gorshelev, V., Weber, M., Chehade, W., and Burrows, J. P.: High spectral resolution ozone absorption cross-sections - Part 2: Temperature dependence, Atmospheric Measurement Techniques, 7, 625–636, https://doi.org/10.5194/amt-7-625-2014, 2014.

Sinreich, R., Merten, A., Molina, L., and Volkamer, R.: Parameterizing radiative transfer to convert MAX-DOAS dSCDs into near-surface box-averaged mixing ratios, Atmospheric Measurement Techniques, 6, 1521–1532, https://doi.org/10.5194/amt-6-1521-2013, https://www.atmos-meas-tech.net/6/1521/2013/, 2013.

https://doi.org/10.5194/amt-2019-204
Preprint. Discussion started: 6 August 2019

Atmospheric Measurement Techniques Discussions

Spurr, R.: LIDORT and VLIDORT: linearized pseudo-spherical scalar and vector discrete ordinate radiative transfer models for use in remote sensing retrieval problems, Light scattering reviews, 3, 229–75, 2008.

Spurr, R., Kurosu, T., and Chance, K.: A linearized discrete ordinate radiative transfer model for atmospheric remote-sensing retrieval, Journal of Quantitative Spectroscopy and Radiative Transfer, 68, 689 – 735, https://doi.org/https://doi.org/10.1016/S0022-4073(00)00055-8, http://www.sciencedirect.com/science/article/pii/S0022407300000558, 2001.

Stocker, T. F., Qin, D., Plattner, G.-K., Tignor, M., Allen, S. K., Boschung, J., Nauels, A., Xia, Y., Bex, B., and Midgley, B.: IPCC, 2013: climate change 2013: the physical science basis. Contribution of working group I to the fifth assessment report of the intergovernmental panel on climate change, 2013.

Thalman, R. and Volkamer, R.: Temperature dependent absorption cross-sections of O_2-O_2 collision pairs between 340 and 630 nm and at atmospherically relevant pressure, Phys. Chem. Chem. Phys., 15, 15 371–15 381, https://doi.org/10.1039/C3CP50968K, 2013.

Toledano, C., Wiegner, M., Garhammer, M., Seefeldner, M., Gasteiger, J., Müller, D., and Koepke, P.: Spectral aerosol optical depth characterization of desert dust during SAMUM 2006, Tellus B, 61, 216–228, https://doi.org/10.1111/j.1600-0889.2008.00382.x, 2009.

Toledano, C., Wiegner, M., Gro, S., Freudenthaler, V., Gasteiger, J., Müller, D., Müller, T., Schladitz, A., Weinzierl, B., Torres, B., et al.: Optical properties of aerosol mixtures derived from sun-sky radiometry during SAMUM-2, Tellus B, 63, 635–648, https://doi.org/10.1111/j.1600-0889.2011.00573.x, https://onlinelibrary.wiley.com/doi/abs/10.1111/j.1600-0889.2011.00573.x, 2011.

Valavanidis, A., Fiotakis, K., and Vlachogianni, T.: Airborne Particulate Matter and Human Health: Toxicological Assessment and Importance of Size and Composition of Particles for Oxidative Damage and Carcinogenic Mechanisms, Journal of Environmental Science and Health, Part C, 26, 339–362, https://doi.org/10.1080/10590500802494538, 2008.

Viana, M., Pey, J., Querol, X., Alastuey, A., de Leeuw, F., and Lükewille, A.: Natural sources of atmospheric aerosols influencing air quality across Europe, Science of The Total Environment, 472, 825 – 833, https://doi.org/https://doi.org/10.1016/j.scitotenv.2013.11.140, http://www.sciencedirect.com/science/article/pii/S0048969713014447, 2014.

Vlemmix, T., Piters, A. J. M., Berkhout, A. J. C., Gast, L. F. L., Wang, P., and Levelt, P. F.: Ability of the MAX-DOAS method to derive profile information for NO_2: can the boundary layer and free troposphere be separated?, Atmospheric Measurement Techniques, 4, 2659–2684, https://doi.org/10.5194/amt-4-2659-2011, https://www.atmos-meas-tech.net/4/2659/2011/, 2011.

Volkamer, R., Spietz, P., Burrows, J., and Platt, U.: High-resolution absorption cross-section of glyoxal in the UV-Vis and IR spectral ranges, Journal of Photochemistry and Photobiology A: Chemistry, 172, 35–46, https://doi.org/http://dx.doi.org/10.1016/j.jphotochem.2004.11.011, 2005.

Wagner, T., Dix, B., Friedeburg, C. v., Fries, U., Sanghavi, S., Sinreich, R., and Platt, U.: MAX-DOAS O_4 measurements: A new technique to derive information on atmospheric aerosols - Principles and information content, Journal of Geophysical Research: Atmospheres, 109, https://doi.org/10.1029/2004JD004904, 2004.

Wagner, T., Burrows, J. P., Deutschmann, T., Dix, B., von Friedeburg, C., Frieß, U., Hendrick, F., Heue, K.-P., Irie, H., Iwabuchi, H., Kanaya, Y., Keller, J., McLinden, C. A., Oetjen, H., Palazzi, E., Petritoli, A., Platt, U., Postylyakov, O., Pukite, J., Richter, A., van Roozendael, M., Rozanov, A., Rozanov, V., Sinreich, R., Sanghavi, S., and Wittrock, F.: Comparison of box-air-mass-factors and radiances for Multiple-Axis Differential Optical Absorption Spectroscopy (MAX-DOAS) geometries calculated from different UV/visible radiative transfer models, Atmospheric Chemistry and Physics, 7, 1809–1833, https://doi.org/10.5194/acp-7-1809-2007, https://www.atmos-chem-phys.net/7/1809/2007/, 2007.

Wagner, T., Deutschmann, T., and Platt, U.: Determination of aerosol properties from MAX-DOAS observations of the Ring effect, Atmospheric Measurement Techniques, 2, 495–512, https://doi.org/10.5194/amt-2-495-2009, 2009.

https://doi.org/10.5194/amt-2019-204
Preprint. Discussion started: 6 August 2019

Wagner, T., Beirle, S., Brauers, T., Deutschmann, T., Frieß, U., Hak, C., Halla, J. D., Heue, K. P., Junkermann, W., Li, X., Platt, U., and Pundt-Gruber, I.: Inversion of tropospheric profiles of aerosol extinction and HCHO and NO_2 mixing ratios from MAX-DOAS observations in Milano during the summer of 2003 and comparison with independent data sets, Atmospheric Measurement Techniques, 4, 2685–2715, https://doi.org/10.5194/amt-4-2685-2011, https://www.atmos-meas-tech.net/4/2685/2011/, 2011.

Wagner, T., Apituley, A., Beirle, S., Dörner, S., Friess, U., Remmers, J., and Shaiganfar, R.: Cloud detection and classification based on MAX-DOAS observations, Atmospheric Measurement Techniques, 7, 1289–1320, https://doi.org/10.5194/amt-7-1289-2014, 2014.

Wagner, T., Beirle, S., Remmers, J., Shaiganfar, R., and Wang, Y.: Absolute calibration of the colour index and O_4 absorption derived from Multi AXis (MAX-)DOAS measurements and their application to a standardised cloud classification algorithm, Atmospheric Measurement Techniques, 9, 4803–4823, https://doi.org/10.5194/amt-9-4803-2016, 2016.

Wagner, T., Beirle, S., Benavent, N., Bösch, T., Chan, K. L., Donner, S., Dörner, S., Fayt, C., Frieß, U., García-Nieto, D., Gielen, C., González-Bartolome, D., Gomez, L., Hendrick, F., Henzing, B., Jin, J. L., Lampel, J., Ma, J., Mies, K., Navarro, M., Peters, E., Pinardi, G., Puentedura, O., Pukite, J., Remmers, J., Richter, A., Saiz-Lopez, A., Shaiganfar, R., Sihler, H., Van Roozendael, M., Wang, Y., and Yela, M.: Is a scaling factor required to obtain closure between measured and modelled atmospheric O_4 absorptions? – A case study for two days during the MADCAT campaign, Atmospheric Measurement Techniques Discussions, 2018, 1–85, https://doi.org/10.5194/amt-2018-238, https://www.atmos-meas-tech-discuss.net/amt-2018-238/, 2018.

Wang, S., Cuevas, C. A., Frieß, U., and Saiz-Lopez, A.: MAX-DOAS retrieval of aerosol extinction properties in Madrid, Spain, Atmospheric Measurement Techniques, 9, 5089–5101, https://doi.org/10.5194/amt-9-5089-2016, 2016.

Wang, T., Hendrick, F., Wang, P., Tang, G., Clémer, K., Yu, H., Fayt, C., Hermans, C., Gielen, C., Müller, J.-F., Pinardi, G., Theys, N., Brenot, H., and Van Roozendael, M.: Evaluation of tropospheric SO_2 retrieved from MAX-DOAS measurements in Xianghe, China, Atmospheric Chemistry and Physics, 14, 11 149–11 164, https://doi.org/10.5194/acp-14-11149-2014, https://www.atmos-chem-phys.net/14/11149/2014/, 2014.

Wiegner, M., Groß, S., Freudenthaler, V., Schnell, F., and Gasteiger, J.: The May/June 2008 Saharan dust event over Munich: Intensive aerosol parameters from lidar measurements, Journal of Geophysical Research: Atmospheres, 116, https://doi.org/10.1029/2011JD016619, d23213, 2011.

Wiegner, M., Madonna, F., Binietoglou, I., Forkel, R., Gasteiger, J., Geiß, A., Pappalardo, G., Schäfer, K., and Thomas, W.: What is the benefit of ceilometers for aerosol remote sensing? An answer from EARLINET, Atmospheric Measurement Techniques, 7, 1979–1997, https://doi.org/10.5194/amt-7-1979-2014, 2014.

Xin, J., Wang, Y., Li, Z., Wang, P., Hao, W. M., Nordgren, B. L., Wang, S., Liu, G., Wang, L., Wen, T., Sun, Y., and Hu, B.: Aerosol optical depth (AOD) and Ångström exponent of aerosols observed by the Chinese Sun Hazemeter Network from August 2004 to September 2005, Journal of Geophysical Research: Atmospheres, 112, https://doi.org/10.1029/2006JD007075, 2007.

Zhang, Z., Wenig, M., Zhou, W., Diehl, T., Chan, K. L., and Wang, L.: The contribution of different aerosol sources to the Aerosol Optical Depth in Hong Kong, Atmospheric Environment, 83, 145–154, https://doi.org/http://dx.doi.org/10.1016/j.atmosenv.2013.10.047, 2014.